Open access • Journal Article • DOI:10.1088/0029-5515/53/10/104007

Overview of physics results from the conclusive operation of the National Spherical Torus Experiment — Source link

S.A. Sabbagh, Joon-Wook Ahn, Jean Paul Allain, R. Andre ...+176 more authors

Institutions: Columbia University, Oak Ridge National Laboratory, Purdue University, Princeton Plasma Physics Laboratory ...+26 more institutions

Published on: 01 Oct 2013 - Nuclear Fusion (IOP Publishing Ltd.)

Topics: Collisionality, Tokamak, Neutral beam injection, Divertor and Microturbulence

Title
Overview of physics results from the conclusive operation of the National Spherical Torus Experiment

Journal
Nuclear Fusion, 53(10)

ISSN
0029-5515

Authors
Sabbagh, SA
Ahn, JW
Allain, J
et al.

Publication Date
2013-10-01

DOI
10.1088/0029-5515/53/10/104007

IOP Publishing and International Atomic Energy Agency Nuclear Fusion

Nucl. Fusion **53** (2013) 104007 (23pp) doi:10.1088/0029-5515/53/10/104007

Overview of physics results from the conclusive operation of the National Spherical Torus Experiment

S.A. Sabbagh[1], J.-W. Ahn[2], J. Allain[3], R. Andre[4], A. Balbaky[1], R. Bastasz[5], D. Battaglia[4], M. Bell[4], R. Bell[4], P. Beiersdorfer[6], E. Belova[4], J. Berkery[1], R. Betti[7], J. Bialek[1], T. Bigelow[2], M. Bitter[4], J. Boedo[8], P. Bonoli[9], A. Boozer[1], A. Bortolon[10], D. Boyle[4], D. Brennan[11], J. Breslau[4], R. Buttery[12], J. Canik[2], G. Caravelli[13], C. Chang[4], N. Crocker[14], D. Darrow[4], B. Davis[4], L. Delgado-Aparicio[4], A. Diallo[4], S. Ding[15], D. D'Ippolito[16], C. Domier[17], W. Dorland[18], S. Ethier[4], T. Evans[12], J. Ferron[12], M. Finkenthal[13], J. Foley[19], R. Fonck[20], R. Frazin[21], E. Fredrickson[4], G. Fu[4], D. Gates[4], S. Gerhardt[4], A. Glasser[22], N. Gorelenkov[4], T. Gray[2], Y. Guo[15], W. Guttenfelder[4], T. Hahm[4], R. Harvey[23], A. Hassanein[3], W. Heidbrink[10], K. Hill[4], Y. Hirooka[24], E.B. Hooper[6], J. Hosea[4], D. Humphreys[12], K. Indireshkumar[4], F. Jaeger[2], T. Jarboe[22], S. Jardin[4], M. Jaworski[4], R. Kaita[4], J. Kallman[4], O. Katsuro-Hopkins[1], S. Kaye[4], C. Kessel[4], J. Kim[25], E. Kolemen[4], G. Kramer[4], S. Krasheninnikov[8], S. Kubota[14], H. Kugel[4], R.J. La Haye[12], L. Lao[12], B. LeBlanc[4], W. Lee[26], K. Lee[17], J. Leuer[12], F. Levinton[19], Y. Liang[17], D. Liu[10], J. Lore[2], N. Luhmann Jr[17], R. Maingi[2], R. Majeski[4], J. Manickam[4], D. Mansfield[4], R. Maqueda[19], E. Mazzucato[4], A. McLean[2], D. McCune[4], B. McGeehan[26], G. McKee[20], S. Medley[4], E. Meier[6], J. Menard[4], M. Menon[27], H. Meyer[28], D. Mikkelsen[4], G. Miloshevsky[3], D. Mueller[4], T. Munsat[29], J. Myra[16], B. Nelson[22], N. Nishino[30], R. Nygren[5], M. Ono[4], T. Osborne[12], H. Park[25], J. Park[4], Y.S. Park[1], S. Paul[4], W. Peebles[14], B. Penaflor[12], R.J. Perkins[4], C. Phillips[4], A. Pigarov[8], M. Podesta[4], J. Preinhaelter[31], R. Raman[22], Y. Ren[4], G. Rewoldt[4], T. Rognlien[6], P. Ross[4], C. Rowley[4], E. Ruskov[10], D. Russell[16], D. Ruzic[21], P. Ryan[2], M. Schaffer[12], E. Schuster[32], F. Scotti[4], K. Shaing[20], V. Shevchenko[28], K. Shinohara[33], V. Sizyuk[3], C.H. Skinner[4], A. Smirnov[23], D. Smith[20], P. Snyder[12], W. Solomon[4], A. Sontag[2], V. Soukhanovskii[6], T. Stoltzfus-Dueck[4], D. Stotler[4], B. Stratton[4], D. Stutman[13], H. Takahashi[4], Y. Takase[34], N. Tamura[24], X. Tang[35], G. Taylor[4], C. Taylor[3], K. Tritz[13], D. Tsarouhas[3], M. Umansky[6], J. Urban[31], E. Untergberg[12], M. Walker[12], W. Wampler[5], W. Wang[4], J. Whaley[5], R. White[4], J. Wilgen[2], R. Wilson[4], K.L. Wong[4], J. Wright[9], Z. Xia[17], D. Youchison[5], G. Yu[8], H. Yuh[19], L. Zakharov[4], D. Zemlyanov[3], G. Zimmer[4] and S.J. Zweben[4]

[1] Department of Applied Physics and Applied Mathematics, Columbia University, New York, NY, USA
[2] Oak Ridge National Laboratory, Oak Ridge, TN, USA
[3] School of Nuclear Engineering, Purdue University, West Lafayette, IN, USA
[4] Princeton Plasma Physics Laboratory, Princeton, NJ, USA
[5] Sandia National Laboratory, Albuquerque, NM, USA
[6] Lawrence Livermore National Laboratory, Livermore, CA, USA
[7] Laboratory for Laser Energetics and Department of Mechanical Engineering, University of Rochester, Rochester, NY, USA

[8] Center for Energy Research, University of California San Diego, La Jolla, CA, USA
[9] MIT Plasma Science and Fusion Center, Cambridge, MA, USA
[10] Department of Physics and Astronomy, University of California, Irvine, CA, USA
[11] Department of Physics, University of Tulsa, Tulsa, OK, USA
[12] General Atomics, San Diego, CA, USA
[13] Department of Physics and Astronomy, The Johns Hopkins University, Baltimore, MD, USA
[14] Department of Physics and Astronomy, University of California, Los Angeles, CA, USA
[15] Institute of Plasma Physics Chinese Academy of Sciences, Hefei, People's Republic of China
[16] Lodestar Research Corporation, Boulder, CO, USA
[17] Department of Electrical and Computer Engineering, University of California, Davis, CA, USA
[18] Department of Physics, University of Maryland, College Park, MD, USA
[19] Nova Photonics, Inc., Princeton, NJ, USA
[20] Department of Engineering Physics, University of Wisconsin, Madison, WI, USA
[21] Center for Plasma-Material Interactions, Department of Nuclear, Plasma and Radiological Engineering, University of Illinois at Urbana-Champaign, IL, USA
[22] PSI Center, Department of Aeronautics and Astronautics, University of Washington, Seattle, WA, USA
[23] CompX, Del Mar, CA, USA
[24] National Institute for Fusion Science, Oroshi, Toki, Gifu, Japan
[25] POSTECH, Pohang, Korea
[26] Dickinson College, Carlisle, PA, USA
[27] Think Tank Inc., Silver Springs, MD, USA
[28] Culham Center for Fusion Energy, Abingdon, Oxfordshire, UK
[29] Department of Physics, University of Colorado, Boulder, CO, USA
[30] Graduate School of Engineering, Hiroshima University, Higashihiroshima, Hiroshima, Japan
[31] Institute of Plasma Physics, AS CR, Prague, Czech Republic
[32] Department of Mechanical Engineering and Mechanics, Lehigh University, Bethlehem, PA, USA
[33] Japan Atomic Energy Agency, Naka, Ibaraki, Japan
[34] Graduate School of Frontier Sciences, The University of Tokyo, Kashiwa, Japan
[35] Los Alamos National Laboratory, Los Alamos, NM, USA

E-mail: sabbagh@pppl.gov

Received 11 December 2012, accepted for publication 2 September 2013
Published 26 September 2013
Online at stacks.iop.org/NF/53/104007

Abstract
Research on the National Spherical Torus Experiment, NSTX, targets physics understanding needed for extrapolation to a steady-state ST Fusion Nuclear Science Facility, pilot plant, or DEMO. The unique ST operational space is leveraged to test physics theories for next-step tokamak operation, including ITER. Present research also examines implications for the coming device upgrade, NSTX-U. An energy confinement time, τ_E, scaling unified for varied wall conditions exhibits a strong improvement of $B_T\tau_E$ with decreased electron collisionality, accentuated by lithium (Li) wall conditioning. This result is consistent with nonlinear microtearing simulations that match the experimental electron diffusivity quantitatively and predict reduced electron heat transport at lower collisionality. Beam-emission spectroscopy measurements in the steep gradient region of the pedestal indicate the poloidal correlation length of turbulence of about ten ion gyroradii increases at higher electron density gradient and lower T_i gradient, consistent with turbulence caused by trapped electron instabilities. Density fluctuations in the pedestal top region indicate ion-scale microturbulence compatible with ion temperature gradient and/or kinetic ballooning mode instabilities. Plasma characteristics change nearly continuously with increasing Li evaporation and edge localized modes (ELMs) stabilize due to edge density gradient alteration. Global mode stability studies show stabilizing resonant kinetic effects are enhanced at lower collisionality, but in stark contrast have almost no dependence on collisionality when the plasma is off-resonance. Combined resistive wall mode radial and poloidal field sensor feedback was used to control $n = 1$ perturbations and improve stability. The disruption probability due to unstable resistive wall modes (RWMs) was surprisingly reduced at very high $\beta_N/l_i > 10$ consistent with low frequency magnetohydrodynamic spectroscopy measurements of mode stability. Greater instability seen at intermediate β_N is consistent with decreased kinetic RWM stabilization. A model-based RWM state-space controller produced long-pulse discharges exceeding $\beta_N = 6.4$ and $\beta_N/l_i = 13$. Precursor analysis shows 96.3% of disruptions can be predicted with 10 ms warning and a false positive rate of only 2.8%. Disruption halo currents rotate toroidally and can have significant toroidal asymmetry. Global kinks cause measured fast ion redistribution, with full-orbit calculations showing redistribution from the core outward and towards $V_\parallel/V = 1$ where destabilizing compressional Alfvén eigenmode resonances are expected. Applied 3D fields altered global Alfvén eigenmode characteristics. High-harmonic fast-wave (HHFW) power couples to field lines across the entire width of the scrape-off layer, showing the importance of the inclusion

of this phenomenon in designing future RF systems. The snowflake divertor configuration enhanced by radiative detachment showed large reductions in both steady-state and ELM heat fluxes (ELMing peak values down from 19 MW m^{-2} to less than 1.5 MW m^{-2}). Toroidal asymmetry of heat deposition was observed during ELMs or by 3D fields. The heating power required for accessing H-mode decreased by 30% as the triangularity was decreased by moving the X-point to larger radius, consistent with calculations of the dependence of $E \times B$ shear in the edge region on ion heat flux and X-point radius. Co-axial helicity injection reduced the inductive start-up flux, with plasmas ramped to 1 MA requiring 35% less inductive flux. Non-inductive current fraction (NICF) up to 65% is reached experimentally with neutral beam injection at plasma current $I_p = 0.7$ MA and between 70–100% with HHFW application at $I_p = 0.3$ MA. NSTX-U scenario development calculations project 100% NICF for a large range of $0.6 < I_p(\text{MA}) < 1.35$.

1. Introduction

Research on the National Spherical Torus Experiment, NSTX [1], targets the development of predictive physics understanding needed to extrapolate plasma transport, stability, power handling, non-inductive sustainment, and advanced control techniques confidently towards the goal of a steady-state Fusion Nuclear Science Facility (ST-FNSF)/Component Test Facility (ST-CTF) [2–4], a pilot plant [5], or DEMO based on the ST [6]. The unique spherical torus (ST) operational space and device geometry are leveraged to extend and test physics theories and technological solutions for next-step ST and tokamak operation, including ITER [7]. Recent research also examines implications for the coming device upgrade, NSTX-U [8], that will double the toroidal field (to 1 T), plasma current (to 2 MA), and neutral beam heating power (to 12 MW) to produce yet unexplored, hotter, high beta ST plasmas at reduced collisionality, ν, for several current diffusion times (up to 5 s pulses). This five-fold increase in pulse length will significantly enhance the device capability to demonstrate and study the stability physics and control needed to sustain both inductive and non-inductively sustained, high beta plasmas in near steady-state conditions. Sustaining stability and control of such plasmas with insignificant fluctuation of plasma stored energy without the use of inductive drive is expected to be especially challenging. Demonstrating and understanding the dependence of high beta plasma transport and stability at reduced collisionality is critical to determining the size and advanced control capabilities needed for an ST-FNSF facility in the role of a CTF [4]. Wall materials and related edge recycling can significantly affect plasma energy confinement and stability, and lithium wall conditioning [9] is investigated in these roles. Advanced instability control and disruption warning techniques are required for disruption avoidance with high reliability. Innovative divertor configurations are needed to handle the high heat and particle fluxes to the device first-wall [10]. Operation with high non-inductive fraction is required to reach a key milestone of NSTX-U—the demonstration of routine fully non-inductive operation over a large operational regime. The impact of non-axisymmetric effects, e.g. on stability and first-wall heat fluxes, including the effect of applied 3D fields, is addressed throughout the research. Similarly, the impact of lithium wall conditioning is examined in several areas including transport and stability. Filling the gaps in our present understanding of these varied, critical areas comprises present NSTX, and future NSTX-U research. These topics are addressed in the present paper.

2. Transport and stability physics at reduced collisionality

2.1. Energy confinement dependence on collisionality

Lower collisionality has been obtained in H-mode plasmas via lithium (Li) conditioning of first-wall components. An increase in energy confinement time, τ_E, has also been reported, most notably in the electron channel [9, 11]. A unified scaling of τ_E with engineering parameters in discharges with/without lithium wall conditioning (lithiated/unlithiated) has not been found. However, such a scaling has been produced by considering a more profound underlying collisionality variation that unifies results for differing wall conditions and that exhibits a strong improvement of toroidal field, B_T-normalized energy confinement with decreasing ν^* [12]. The MAST ST has also reported a τ_E scaling dependence on plasma current and toroidal field that is significantly different than that found in conventional tokamak scalings [13] and have examined the dependence of τ_E on collisionality [14]. This determined dependence may influence the design and construction of an ST-FNSF significantly, as such a device will operate at collisionalities of at least an order of magnitude less than the operating range of NSTX. The relation between τ_E and collisionality was studied using data from NSTX I_p and B_T scans of both lithiated and unlithiated plasmas. In these scans, the gyrofrequency $\Omega \propto 1/B_T$ varied considerably as did ρ^*, with the latter varying by almost a factor of two across the range of collisionality. The Ω variation is accounted for by normalizing τ_E as $B_T\tau_E$. For this analysis, a dataset was sub-selected which minimized the safety factor q and plasma beta, β variations ($\beta \equiv 2\mu_0\langle p\rangle/B_0^2$ where p is the plasma pressure and B_0 is the vacuum toroidal magnetic field); the data were constrained to $2 < q(r/a = 0.5) < 2.5$, and a β range of between 8.5% and 12.5%. While this was the full range of the β variation, most of the data lie in the range from 10.5% to 12.5% (where r is the plasma minor radial coordinate). The data set spans a factor of four variation in normalized electron collisionality, ν_e^* (at $r/a = 0.5$), with a minimum value of 0.05. Normalized confinement times for the ν_e^* and Li scans are shown in figure 1. Note that the lithiated data in figure 1(a) and the set in figure 1(b) are from different scans. While the data are plotted as a function of electron collisionality, the ion collisionality varied also in a manner similar to the electron collisionality.

The normalized energy confinement time is well-ordered by ν_e^* and unifies the scaling of discharges with both types of wall conditioning. The scaling $B_T\tau_E \propto \nu_e^{*-0.79}$ is found for all discharges (figure 1), and a similar strong inverse

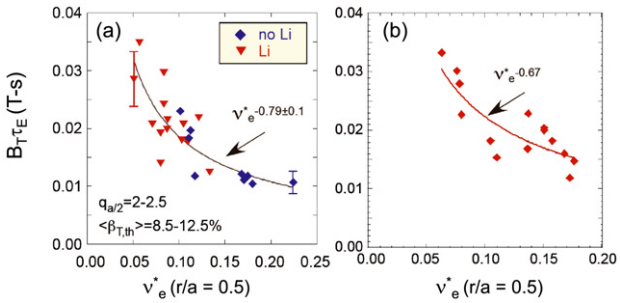

Figure 1. Normalized energy confinement time versus collisionality for (*a*) ν^*_e scan and (*b*) Li scan.

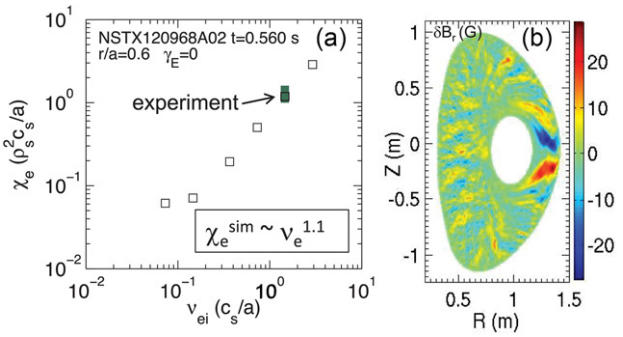

Figure 2. (*a*) Computed electron diffusivity versus electron collisionality; (*b*) poloidal cross section plot of computed radial B field fluctuation.

scaling $\propto \nu^{*-0.67}_e$ with is found for lithiated discharges alone. Local T_e variation due to profile broadening is the most influential factor in varying ν^*_e. Including a variation of the normalized gyroradius ρ^* yields a considerably stronger favourable increase of $B_T\tau_E$ with decreased ν^*_e, assuming either a Bohm, or gyroBohm dependence. Ion transport, near neoclassical at high collisionality, became more anomalous at lower collisionality due to the growth of hybrid trapped electron modes/kinetic ballooning modes (TEMs/KBMs) in the outer regions of the plasma [15].

2.2. Gyrokinetic simulations of electron thermal transport

The broad parameter space of the ST, yielding a wide range of possible microinstabilities, provides a unique laboratory for developing an integrated understanding of transport. The dependence of electron thermal transport on electron collisionality, ν_{ei}, is examined for plasmas with different underlying microinstabilities. Plasmas with sufficiently high beta and collisionality are computed to be linearly unstable only to microtearing modes in the core confinement region (r/a = 0.4–0.8) [16]. Nonlinear gyrokinetic simulations using the Eulerian delta-f gyrokinetic code GYRO [17, 18] have been pursued to calculate the magnitude and scaling of microtearing transport. The local simulations use realistic geometry extracted from magnetohydrodynamic (MHD) equilibrium reconstructions [19] and include kinetic ions and electrons, collisions (pitch-angle scattering) and electromagnetic perturbations. In the absence of $E \times B$ shear, the nonlinear simulations predict electron heat transport that matches the experimental electron thermal diffusivity, χ_e, [20] for the experimental value of collisionality (figure 2(*a*)). The computed transport is dominated by magnetic flutter with high $\delta B_r/B \sim 0.1\%$ (figure 2(*b*)) which leads to stochastic field lines [21]. Furthermore, the simulations predict a reduction of electron heat transport at lower collisionality with a computed scaling $\chi_e \sim \nu^{1.1}_e$ [22] that is consistent with the experimentally derived $B_t\tau_E \sim \nu^{*-0.79}_e$ (section 2.1). The transport analyses for the discharges in figure 1 (described in greater detail in [12]) demonstrate a significant correlation between the experimental χ_e at $r/a = 0.6$–0.7 and the global confinement times, suggesting that the microtearing mode may in fact be an important component in describing the confinement scaling. The range of minor radial positions used in these calculations is smaller than the position of the steep gradient region of the pedestal.

This simple interpretation is complicated by the observation that the microtearing transport is predicted to be stiff, with the electron temperature gradient (ETG) indicating that the scaling of the stability threshold should also be important. Additionally, the local $E \times B$ shearing rate is similar to the linear growth rate and the corresponding transport is suppressed below experimental levels when it is included in the nonlinear simulations. (In contrast, related nonlinear microtearing simulations for conventional aspect ratio devices predict that strong $E \times B$ shear does not significantly reduce transport [23, 24]. The reason for this difference is not yet understood.) Refinements in numerical resolution might reduce this discrepancy, as will improvements in physics model assumptions. For example, non-local effects occurring at finite $r_* = \rho_s/a$ could lead to quantitative changes in predicted transport as the linear growth rates become much larger than local $E \times B$ shearing rates with increasing minor radius. Global electromagnetic simulations are needed to verify this effect, although they are considerably more computationally expensive owing to the fine radial resolution required to resolve high order rational surfaces at increasing magnetic shear further out in the plasma [22].

In high beta plasmas, KBM are also predicted to occur further out in the plasma ($r/a \geqslant 0.8$, towards the pedestal top). At lower collisionality, microtearing modes often become weaker (due to broadening of the T_e profile), and the extent of the KBM can move in as far as $r/a = 0.7$ due to changes in both the density and temperature profiles (the KBM is sensitive to the total pressure gradient.) In many instances this computed mode scales similarly to the TEM (driven by ∇n and ∇T_e, is insensitive to ∇T_i, is stabilized by increasing ν_e) except it is sensitive to variations in beta, exhibiting a threshold similar to a KBM. Nonlinear GYRO simulations of such modes, called 'hybrid' TEMs/KBMs [15] predict significant electron thermal transport with nearly equal contributions from both electrostatic potential and compressional magnetic perturbations ($\delta B_\parallel/B \sim 0.08\%$). KBM simulations also predict substantial ion heat flux, consistent with the observation that experimental ion thermal diffusivities become increasingly anomalous at low collisionality in the ν^*_e scaling experiments described in section 2.1.

At lower beta, ETG instabilities are often found to be unstable and nonlinear simulations predict significant electron transport. However, a negligible dependence of electron transport with collisionality is found from these simulations,

which is inconsistent with the strong dependence of χ_e on ν_e found experimentally. Instead, the accumulation of small differences in other parameters may lead to the overall change in confinement. For example, simulations at slightly different radii illustrate the predicted ETG transport is sensitive to local variations in density gradient [25, 26].

In neutral beam injection (NBI)-heated L-mode plasmas, a computed reduction of χ_i and χ_e is consistent with $E \times B$ shear stabilization of low-k turbulence, which in turn reduces the high-k fluctuations nonlinearly, consistent with high-k measurements [27]. RF-heated L-mode plasmas have also been used to investigate the physics of ETG turbulence. Electron internal transport barriers (e-ITBs) have been found to occur with strong negative magnetic shear ($s < -0.5$). For a large collection of discharges, both the large local ETGs (much larger than the linear ETG threshold) and the small turbulence intensity found from high-k scattering measurements are strongly correlated with the largest magnitudes of negative magnetic shear [28]. Non-local GYRO simulations verify that the ETG turbulence and transport is suppressed with strong negative magnetic shear in the region of the e-ITB [29]. Electron-scale turbulence has been observed in low β plasmas with the high-k scattering diagnostic [26, 30]. The local electron beta, β_e, at the measurement location of the high-k scattering system is about 2%, in contrast to 8% in plasmas with high β_e [31]. Linear gyrokinetic simulations show that the ETG mode is linearly unstable in these low β plasmas [26].

2.3. Resistive wall mode stability dependence on collisionality

Past NSTX research has established a new understanding of resistive wall mode (RWM) [32] stability by making quantitative correlation between experiments reaching the mode marginal stability point and kinetic RWM stabilization theory [33–36]. This model has important implications for next-step devices operating at reduced collisionality. Early RWM stabilization models relied solely on plasma collisionality as the stabilizing energy dissipation mechanism, therefore always yielding reduced stability at reduced collisionality—a negative result for future devices. The present kinetic RWM stabilization theory changes this significantly, yielding a more complex stability picture. As before, stabilizing effects of collisional dissipation are reduced at lower ν, but new stabilizing resonant kinetic effects can be enhanced. Generally, stronger resistive wall mode stabilization occurs near broad dissipative kinetic resonances (which depend on the plasma rotation profile—both magnitude and shape) and this stabilization increases with decreasing collisionality. However, in stark contrast, the plasma stability has almost no dependence on collisionality when the plasma is off-resonance (see figure 3). In this figure, ν and ω_ϕ^{exp} represent NSTX experimental values in high beta plasmas, and kinetic RWM stability calculations producing the mode growth rate are made using the MISK code [37]. In these calculations both the influence of the bulk plasma on the kinetic effects (e.g. the precession drift resonances, and bounce harmonic resonances [33]) and the effect of the fast particle population [38] are included in the computation of the RWM growth rate. These theoretical results can be compared to

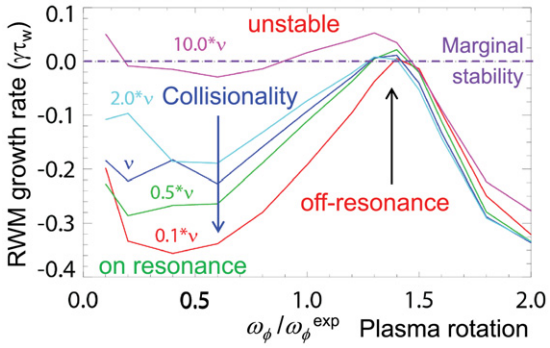

Figure 3. MISK computed kinetic RWM $n = 1$ stability versus plasma rotation for varying collisionality.

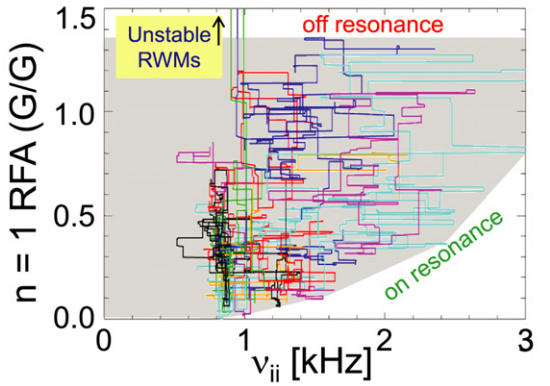

Figure 4. $n = 1$ RFA amplitude versus ν_{ii}, showing a relatively large change at low RFA ('on resonance') versus almost no change at high RFA.

experiments that utilized $n = 1$ active MHD spectroscopy [39] diagnosis (which uses $n = 1$ resonant field amplification (RFA) of a low frequency (40 Hz) applied $n = 1$ tracer field) to directly measure RWM stability [40]. These experiments indicate the expected gradients in RWM stability for plasmas with high $5.5 < \beta_N/l_i < 13.5$ (most are above the $n = 1$ ideal no-wall stability limit) (figure 4) as a function of ion collisionality. Each trace in the figure shows the variation of the RFA amplitude over each discharge evolution for 20 plasmas shots, over which the ion collisionality, ν_{ii}, is varied by a factor of 5 in the range $0.6 < \nu_{ii}(\text{kHz}) < 3$. The theoretically expected gradients in kinetic RWM stability are generally reproduced by the shape of the upper and lower boundaries of the measured $n = 1$ RFA amplitude. At high $n = 1$ RFA amplitude (the upper boundary), the plasma rotation is further from stabilizing kinetic resonances (off-resonance), and there is almost no change in RWM stability (indicated by the high, and near constant $n = 1$ RFA amplitude) versus ν_{ii}. This resembles the behaviour shown by theory in figure 3 labelled 'off-resonance' as ν is varied. These plasmas are near marginal stability, and some become experimentally unstable, as labelled in figure 4. During periods of low $n = 1$ RFA amplitude during the discharge evolution (the lower boundary), the plasma has greater stabilization by kinetic resonances, and there is a clear increase in RWM stability (decrease in $n = 1$ RFA amplitude) as ν_{ii} is decreased. This behaviour is similar to that shown by theory in figure 3 when the plasma

is 'on-resonance' and ν is decreased. The definition of RFA used in this analysis is $A_{\mathrm{RFA,s}} = B_{\mathrm{p,s}}^{\mathrm{plasma}}/B_{\mathrm{p,s}}^{\mathrm{applied}}$, where $B_{\mathrm{p}}^{\mathrm{plasma}}$ is the poloidal field generated by the plasma, $B_{\mathrm{p}}^{\mathrm{applied}}$ is the applied poloidal field generated by the dominantly $n = 1$ tracer field, and subscript s denotes the values at the location of the RWM sensors. Note that $B_{\mathrm{p}}^{\mathrm{plasma}}$ does not contain the applied $n = 1$ field—it is compensated from the sensor measurements. In this analysis, the field, and the applied currents generating them are considered complex variables of the form $|\xi(t)|e^{-in\phi(t)}$, where $|\xi(t)|$ and $\phi(t)$ are the RFA amplitude and phase. This definition is consistent with that used for DIII-D [39], and other NSTX experiments [41]. Twelve RWM sensors are used in the RFA analysis. Here, ν_{ii} is averaged over $0.55 < \psi_{\mathrm{N}} < 0.75$ of the profile, inside of the pedestal, and ψ_{N} is the normalized poloidal flux, $(\psi - \psi_0)/(\psi_{\mathrm{a}} - \psi_0)$, where subscript 'a' represents the plasma edge, and '0' represents the magnetic axis.

3. Transport and stability of the H-mode pedestal

3.1. Effects of lithium wall conditioning and edge localized mode stabilization

Plasma characteristics change nearly continuously with increasing Li evaporation [42], even after complete edge localized mode (ELM) suppression [43], with no Li accumulation in the core [44]: global energy confinement parameters improve (figure 5) and edge transport declines [45], ELM frequency is reduced, or the mode stabilizes completely [46]. In laboratory experiments, the role of oxygen is found to be key to understanding deuterium retention of Li-coated graphite as expected from quantum-classical simulations, and may explain the threshold Li amount required to generate the observed positive plasma effects [47]. While ELM-free discharges using lithium wall conditioning have very low (<0.1%) core Li concentration, carbon accumulation can be significant with core concentration up to 10% as a result of ELM suppression. The neoclassical codes NCLASS [48] and NEO [49] were used to calculate neoclassical impurity transport coefficients for carbon and lithium. The two codes consistently indicated higher neoclassical particle diffusivity for lithium (about an order of magnitude) due to the presence of a high concentration carbon background. Differences between the two codes were observed only in the core region ($r/a \leqslant 0.5$) where NEO predicted an enhancement of radial transport coefficients due to finite toroidal rotation effects (neglected in NCLASS). The difference between the experimental carbon and lithium density profile shape between $r/a = 0.8$ and $r/a = 1.0$ indicated that up to a factor of ~10 difference in the carbon and lithium core densities can be attributed to core/edge radial transport. While the difference in neoclassical transport between carbon and lithium is enough to explain the observed differences in the core, the neoclassical effect is reduced as a result of the apparent anomalous behaviour of carbon in the plasma edge [50]. The extremely low experimental density ratio $n_{\mathrm{Li}}/n_{\mathrm{C}} \sim 1\%$ suggested that a reduction of the edge lithium impurity source of an order of magnitude with respect to the carbon source was further needed in order to reproduce the experimental results. This can be attributed to the different poloidal distribution of carbon and lithium sources as well as to the better scrape-off layer (SOL) screening of lithium divertor impurities.

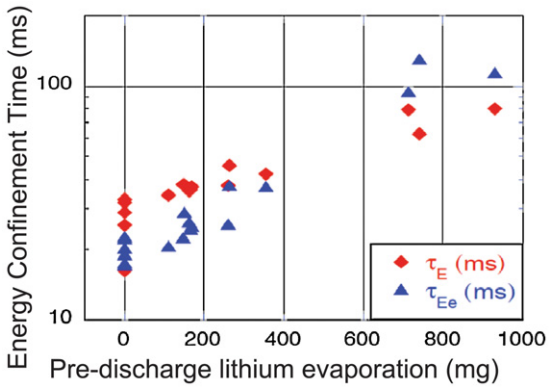

Figure 5. Increase of total, and electron energy confinement time with increased pre-discharge lithium evaporation.

Examination of plasmas with different amounts of pre-discharge Li evaporation provides insight into the subsequent pedestal expansion and ELM suppression physics. The mechanism responsible for ELM avoidance is clarified by profile and stability analysis. Lithium conditioning of the wall reduces recycling and core fuelling, thereby reducing density and its gradient near the separatrix. The degree of this density profile modification changes continuously via the amount of lithium evaporation and resulting recycling control. The pressure gradient and bootstrap current near the separatrix are reduced exclusively by the density change, as the temperature gradient is unaffected. This leads to a computed stabilization of kink/peeling modes thought to be responsible for the ELMs. A surprising and beneficial facet is the continued growth of the edge transport barrier width in these circumstances, leading to 100% higher plasma pressure at the approximate top of the n_{e} profile barrier at the highest level of pre-discharge Li evaporation. Analysis shows the pressure gradient and associated bootstrap current are maintained below the edge stability limit, thus avoiding ELMs. This allows the H-mode edge transport barrier to expand farther in, and in such a way that peeling mode stability improves as a result of the inward shift of the bootstrap current [51]. Linear gyrokinetic calculations have been performed using the GS2 code [45, 52]. Although the local approximation used in this code is not appropriate for ion scale turbulence within the pedestal (where the ion gyroradius is a significant fraction of the gradient scale lengths), it is applicable for electron-scale fluctuations and for ion scales at the pedestal top where the gradients are modest. These simulations show that ETG modes are destabilized in the region near the separatrix $0.95 < \psi_{\mathrm{N}} < 1.0$ when lithium is used. These may play a role in the stiff electron temperature profile observed near the separatrix, which persists even as the density is reduced by the reduction in the particle source caused by lithium wall conditioning. Further, calculations show that microtearing modes are unstable in at the top of the pedestal without lithium. Increasing the local density gradient can be stabilizing to these modes (at fixed β). While the cause is not yet fully understood, it is observed that when lithium wall conditioning is used in these plasmas, the density pedestal broadens substantially, so that the density gradient increases in the range $0.8 < \psi_{\mathrm{N}} < 0.95$ (figure 6). This is

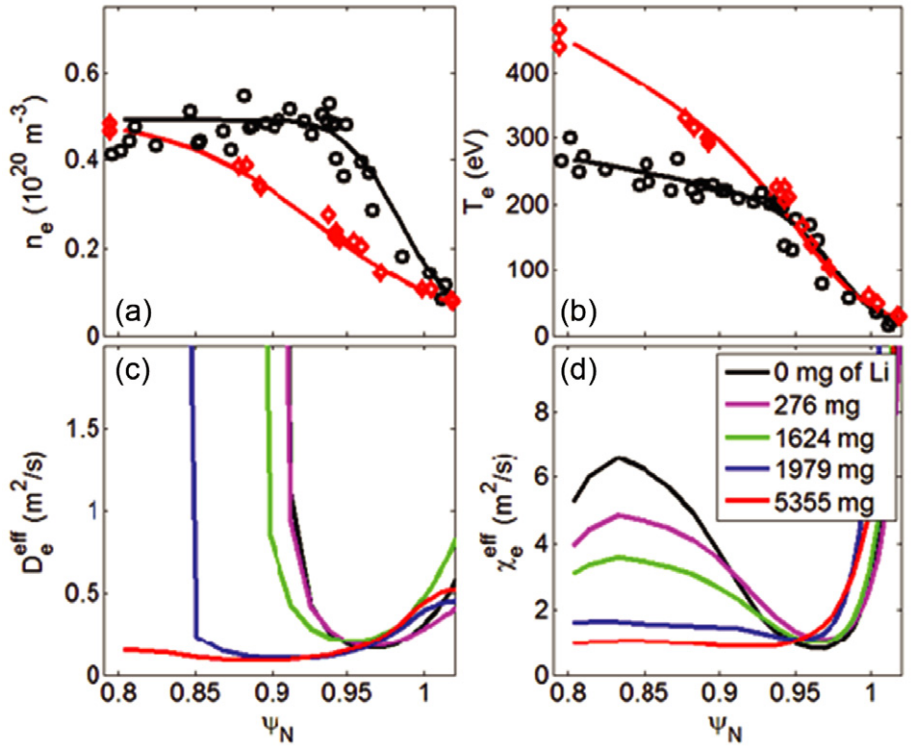

Figure 6. Profiles of (*a*) n_e, (*b*) T_e, without (black circles) and with 5355 mg of lithium deposition (red diamonds) and (*c*) D_e^{eff} and (*d*) χ_e^{eff} (from the SOLPS code) as the amount of lithium is varied.

due to a reduction in the particle transport (the SOLPS code computation of D_e^{eff} is reduced), and cannot be accounted for simply based on the changes to the source profile with lithium [45]. This increase in density gradient is stabilizing to microtearing modes, yielding strongly reduced growth rates as the density pedestal expands inwards and the gradient is increased, which may contribute to the reduction in thermal transport that has been inferred in this region. This qualitative picture of microtearing mode stabilization by the inward growth of the density pedestal is similar to that reported for MAST plasmas [53].

Liquid lithium divertor (LLD) operation showed that despite a nominal liquid level exceeding the capillary structure capacity and peak current densities into the plasma-facing surface exceeding 100 kA m^{-2}, no macroscopic ejection events were observed. In addition, no substrate line emission was observed during normal operations indicating the lithium provides protection of the molybdenum porous layer. Impurity emission from the divertor suggests that the plasma is interacting with impurity-contaminated lithium whether diverted on the LLD or not. A database of LLD discharges was analysed to consider whether there is a net effect on the discharges over the range of total deposited lithium in the machine. Examination of H-97L energy confinement scaling indicates that performance was constant throughout the run, consistent with the hypothesis that it is the quality of the surface layers of the lithium that impact performance. The accumulation of impurities suggests a fully flowing liquid lithium system to obtain a steady-state lithium plasma-facing surface on timescales relevant to NSTX [54]. Surface analysis experiments show oxide coverage of plasma-facing components (PFCs) is expected in 10 s of seconds from residual H_2O at typical NSTX between-discharge pressures $\sim 1 \times 10^{-7}$ Torr. These short observed reaction times motivate flowing Li PFCs.

3.2. Pedestal width scaling and ELM stability calculations

Edge pedestal profiles and associated ELM stability are important for achieving high core fusion gain in next-step devices [55–58]. Peeling–ballooning modes are hypothesized to set an upper limit on the pedestal height. Recently, attention has been placed on computing the bootstrap current profile more accurately in the steep pressure gradient region of the edge pedestal using the XGC0 code [59], to improve existing stability calculations [60]. The XGC0 calculated magnitude of the bootstrap current profile is significantly larger than that computed using the Sauter model in the pedestal region of NSTX plasmas, reaching a value that is twice as large as the Sauter model (figure 7). Using a set of fixed boundary kinetic equilibrium reconstructions during the last part of the ELM cycle, the stability of equilibria similar to those described in section 3.1 is computed using the ELITE MHD stability code (figure 8). Experimental current density and pressure gradient points are shown using the Sauter and XGC0 bootstrap current models. The computed stability contours, produced using the XGC0 current profile, show the marginal stability point to be within error bars of the XGC0 point. Present results indicate that the pedestal pressure is limited by the proximity to the kink/peeling instability limit. The significantly larger bootstrap current computed using the XGC0 model compared to the Sauter model puts the experimental point closer to the kink/peeling mode instability limit. This result may solve the long-standing discrepancy that the normalized current density

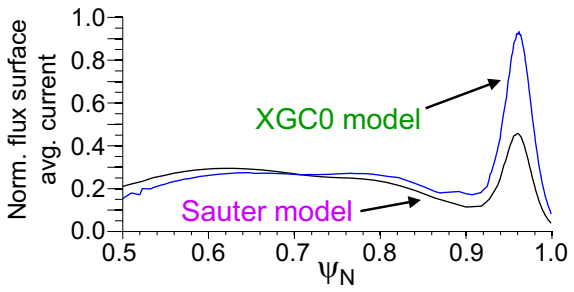

Figure 7. Comparison of normalized flux surface averaged bootstrap current profile for Sauter and XGC0 bootstrap current profile models.

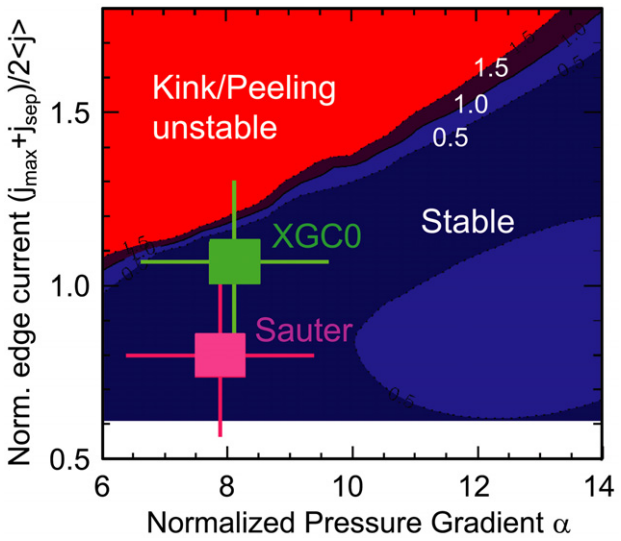

Figure 8. Contours of peeling–ballooning mode growth rate divided by the ion diamagnetic frequency $\omega_i^*/2$ versus normalized current density and pressure gradient.

point can be far from the marginal stability contour computed for NSTX plasmas using the Sauter model (up to an order of magnitude different in the ratio of the peeling/ballooning mode growth rate to the ion diamagnetic frequency $\omega_i^*/2$) when ELMs are destabilized [59]. PEST calculations of $n = 2$–4 modes indicate a maximum growth rate for the $n = 3$ mode. The toroidal mode spectra of ELM activity has not been fully evaluated in NSTX, and measurement of n numbers greater than about 5 is not possible. Filamentary structure of ELM precursor activity has been observed during type-III ELMs, which exhibits relatively low toroidal mode numbers between 2–4 [61].

The pedestal width in tokamaks and STs is thought to be set by KBM [62], with the expected scaling $(\beta_p^{ped})^{0.5}$, where β_p^{ped} is the local poloidal beta using the pressure measured at the pedestal top. This scaling has been reported in several tokamaks including DIII-D, C-Mod, and the MAST ST [63], but the best fit to the NSTX data indicates a significantly stronger scaling, closer to linear in β_p^{ped} (figure 9) [64]. Also, although past analysis using KBM constraints in the ballooning critical pedestal model [62] have yielded a $(\beta_p^{ped})^{0.5}$ scaling for the pedestal width in tokamaks, recent analysis for NSTX has shown a $(\beta_p^{ped})^{0.8}$ dependence (figure 9). It is noted that NSTX

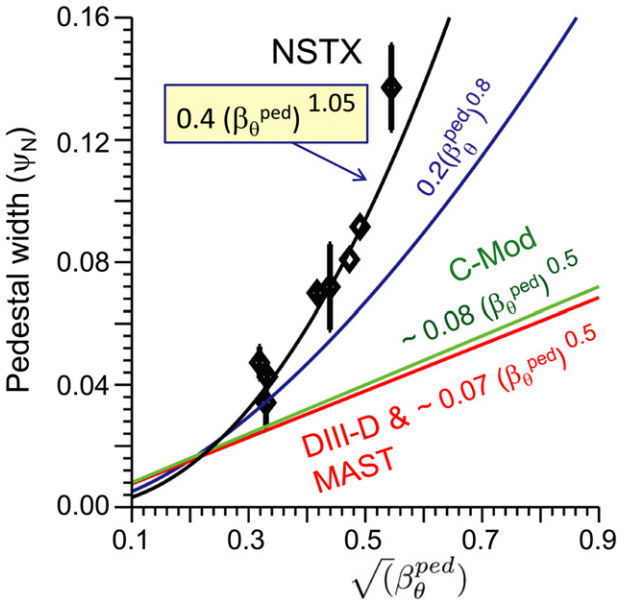

Figure 9. Pedestal width versus $(\beta_p^{ped})^{0.5}$, showing a near linear dependence on β_p^{ped} in NSTX.

has stronger shaping than MAST, and that MAST research claims that the plasmas are ballooning mode-limited [65] as opposed to NSTX which is computed to be peeling mode-limited. As NSTX and MAST have similar aspect ratio, the use of lithium wall conditioning in NSTX may also be an important factor as it leads to the pedestal expansion observed as the amount of pre-discharge lithium is increased. The Thomson scattering diagnostic on NSTX is sufficient to resolve the pedestal widths shown in figure 9, the points with pedestal width of about 0.07 in normalized poloidal flux corresponding to 4 cm, with error bars of about 1 cm.

3.3. Turbulence measurements and characterization in the pedestal region

Beam-emission spectroscopy (BES) [66] measurements have been used to measure spatial and temporal properties of ion-scale turbulence in ELM-free, MHD quiescent H-mode discharges. In the steep gradient region (the lower portion) of the pedestal, measured poloidal correlation lengths of the turbulence, $L_c \sim 10\rho_i$, (ρ_i is the ion gyroradius), wavenumbers $k_\theta \rho_i \sim 0.2$, and normalized decorrelation time $\tau_d/(a/c_s) \sim 5$, where c_s is the sound speed. The sightlines used for the BES system minimize ion density and temperature variation in the measurement volume in the poloidal direction, yielding reliable measurement of the poloidal correlation length. Point spread function calculations indicate image distortion from field-line misalignment and atomic state lifetimes are minor [66]. Regression analysis and model aggregation identified parametric scalings among turbulence quantities and transport-relevant plasma parameters. For systems with complex inter-dependencies, such as plasma turbulence and transport, model aggregation can be preferable to single model selection because single model selection introduces subjective preferences among numerous statistical metrics and plasma parameters, model aggregation identifies more parametric scalings than a single model, and model aggregation

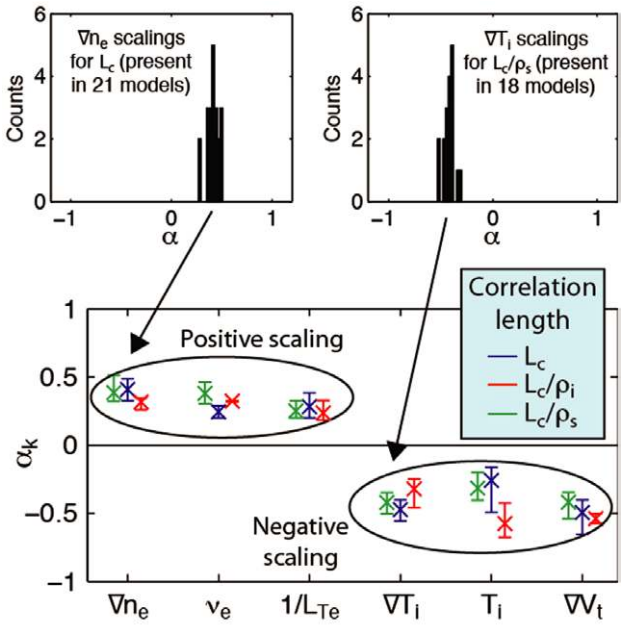

Figure 10. Linear scaling coefficients for poloidal correlation length, L_c, L_c/ρ_i, and L_c/ρ_s, based on BES turbulence measurements in the steep gradient region of H-mode profiles.

identifies scalings that remain valid across a variety of model scenarios and constraints [67, 68]. Figure 10 shows a subset of linear scaling coefficients (α_k) for poloidal correlation length quantities. Model aggregation produces a distribution of scaling coefficients that cover a variety of model scenarios. For example in figure 10, 21 models for L_c, each with different constraints, contain a ∇n_e term. Collectively, the models indicate a positive scaling ($\alpha \approx 0.4$) between L_c and ∇n_e. The L_c increases and k_θ decreases at higher ∇n_e and lower ∇T_i. As shown in figure 10 (further described in [67, 68]), the observed scalings are partially consistent with turbulence caused by trapped electron instabilities, partially consistent with KBM and microtearing mode turbulence, and notably, least consistent with ion temperature gradient (ITG) turbulence.

Investigations were also conducted in ELMing plasmas examining the steep density gradient region, and the region at the top of the pedestal. Characterization of radial edge density fluctuations during the time period between ELM events (inter-ELM phases) was made possible by an array of fixed-frequency quadrature reflectometers allowing for excellent coverage of the pedestal region [69]. Reflectometer measurements were made in both the steep density gradient region, and up to 7 cm (12% of the minor radius) inside of the steep gradient region (at the pedestal top). The radial correlation lengths were computed using a Gaussian fit to the measured correlation function for the data from the steep gradient region, and an exponential fit for the data taken at the top of the pedestal. The poloidal spatial structure of these fluctuations was measured by the BES diagnostic at the pedestal top. Examining the variation of the correlation length over an ELM cycle, the radial correlation length increased at the top of the pedestal by a factor of 2 during the last 50% of the ELM cycle reaching seven times the ion gyroradius at this position, implying increased radial transport (figure 11). In contrast, the correlation length

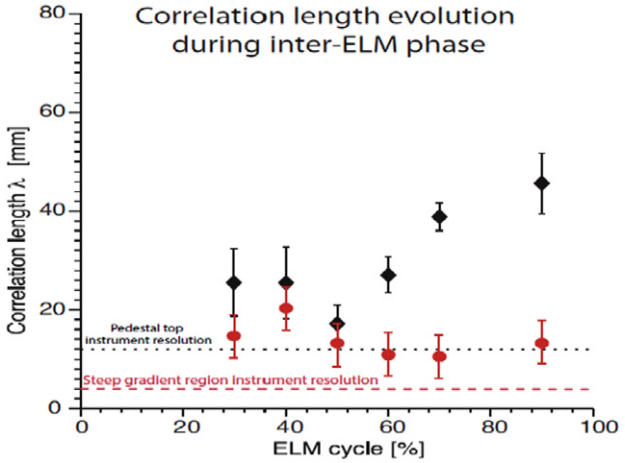

Figure 11. Evolution of electron density fluctuation radial correlation length in the pedestal: pedestal top (black diamonds) and steep gradient region (red circles).

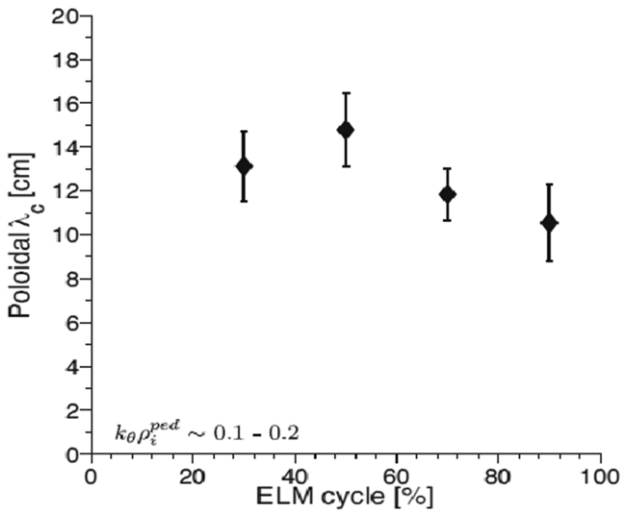

Figure 12. Inter-ELM poloidal correlation length evolution measured using the BES diagnostic.

remained unchanged through the ELM cycle in the steep gradient region. BES measurements also show a large, and relatively constant poloidal correlation length over the ELM cycle (figure 12). The edge density fluctuations in the pedestal top region during the ELM cycle clearly show anisotropic fluctuations and spatial scales $(2/\lambda_\perp)\rho_i^{ped}$ ranging from 0.2 to 0.7 that propagate in the ion diamagnetic drift direction, indicative of ion-scale microturbulence compatible with ITG (including hybrid TEM) and/or KBM instabilities. Here, the perpendicular wavelength, $\lambda_\perp$, is obtained from combining the measured radial and poloidal correlation lengths from the reflectometer and BES diagnostics ($k_\perp = (k_\theta^2 + k_r^2)^{0.5}$). Group velocities determined from the time lags between BES channels are in the ion diamagnetic direction. These are measurably larger in magnitude than the $E_r \times B_\parallel$ velocities at the pedestal top (inferred from charge-exchange recombination spectroscopy (CHERS) carbon ion distribution force balance), and have opposite sign (are in the electron diamagnetic direction) (figure 13). When the BES velocity measurements are combined with the $E \times B$ velocities, the result show that

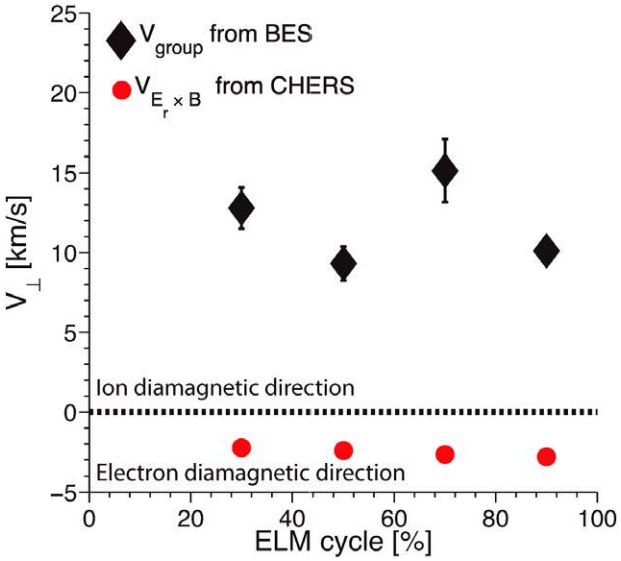

Figure 13. Group velocity of density fluctuations versus time during an ELM cycle. Diamonds (black) show the group velocities based on time lags between BES channels. Additionally, dots (red) show that the $E_r \times B_{\|}$ velocity inferred by CHERS measurements is significantly smaller. When combined, the fluctuation propagation remains in the ion diamagnetic drift direction.

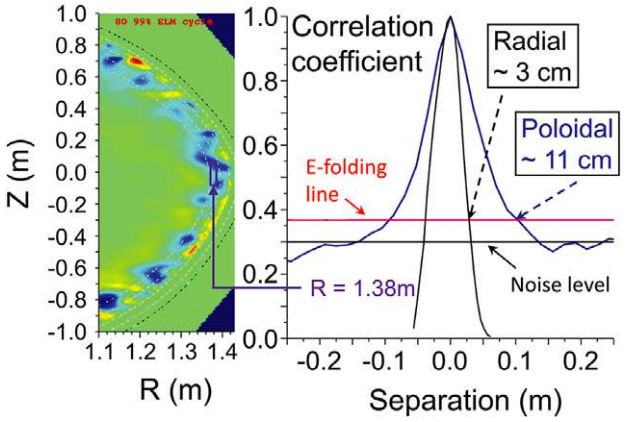

Figure 14. Electrostatic potential fluctuations in the edge region computed from XGC1 simulations showing ITG fluctuations (left) yield radial and poloidal correlation lengths in the range of the measured values from reflectometry and BES diagnostics (right).

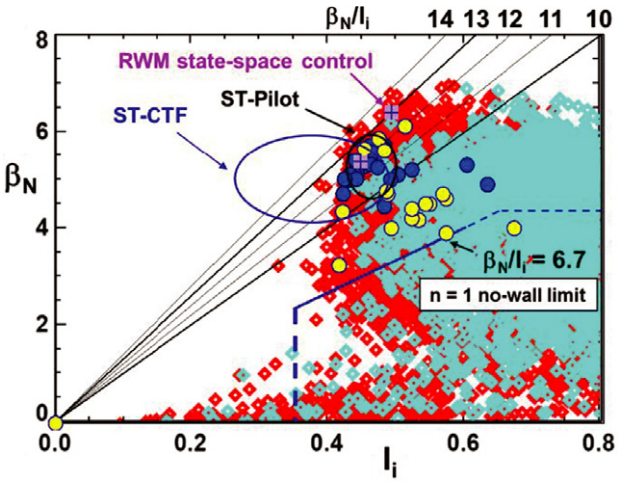

Figure 15. High β_N, low l_i operational space. Red/cyan points indicate plasmas with/without $n = 1$ active RWM control. Blue circles indicate stable long-pulse plasmas with active RWM control; yellow indicates disruptions.

the fluctuations propagate in the ion diamagnetic direction in the plasma frame. This is contrary to observations on DIII-D where both velocities have the same direction [64]. The measured density fluctuation correlation lengths (radial: 2–4 cm; poloidal: 10–14 cm) were compared to nonlinear gyrokinetic simulations (XGC1 code) [70] (figure 14), which show computed correlation lengths of 3 cm (radial) and 11 cm (poloidal). In these simulations, which consider ion dynamics (ITG modes, which intrinsically propagate in the ion diamagnetic drift direction) and do not consider collisions and flows, electrostatic potential fluctuations form with correlation lengths matching the experimentally measured values. Note that electromagnetic fluctuations are not yet considered in these calculations of the pedestal region. The spatial range of the measured fluctuations covered 7.5 cm in the radial direction, and 16 cm in the poloidal direction. The fluctuation results presented here are shown to be ion scale turbulence consistent with KBM instabilities. This is seemingly consistent with recent DIII-D measurements of high frequency modes with characteristics predicted for KBMs in the pedestal region of an otherwise quiescent plasma [71].

4. Macroscopic stability and control at high β, disruption prediction and characteristics

4.1. High beta operation and reduced disruptivity

Next-step STs and steady-state advanced tokamaks both aim to operate continuously at high normalized beta, $\beta_N \equiv 10^8 \langle \beta_t \rangle a B_0 / I_p$, ($\beta_t \equiv 2\mu_0 \langle p \rangle / B_0^2$) and high non-inductive current fraction (NICF). A high bootstrap current fraction yields a broad current profile, corresponding to low plasma internal inductance, l_i. This is favourable for efficient non-inductive operation, but is generally unfavourable for global MHD mode stability, reducing the ideal $n = 1$ no-wall beta limit, $\beta_N^{\text{no-wall}}$. Past high β_N operation with l_i typically in the range $0.6 < l_i < 0.8$ has an $n = 1$ $\beta_N^{\text{no-wall}}$ computed by the DCON code to be 4.2–4.4 [72]. Operation at β_N up to 7.4 and $\beta_N / l_i > 13.5$ has now been demonstrated transiently, with pulse-averaged β_N (averaged over constant plasma current), $\langle \beta_N \rangle_{\text{pulse}} > 5.5$ in low l_i plasmas in the range $0.4 < l_i < 0.6$ with active $n = 1$ mode control (figure 15). Pulse-averaged values of (l_i, β_N) now intercept the higher l_i portion of the planned operational ranges for ST-CTF and ST-Pilot plants. Especially important is that the ideal $n = 1$ no-wall stability limit is significantly reduced at these low l_i values, so that β_N now exceeds the DCON computed $\beta_N^{\text{no-wall}}$ for the experimental equilibrium reconstructions of these plasmas by up to a factor of two. In addition, synthetic variations of the pressure profile for plasmas with $l_i \sim 0.38$ show these equilibria to be at the purely current-driven ideal kink stability limit, as they are computed to be ideal unstable at all values of $\beta_N > 0$. In this operational regime, passive or active kink and resistive wall mode stabilization is therefore critical. The disruption probability due to unstable RWMs was reduced from 48%

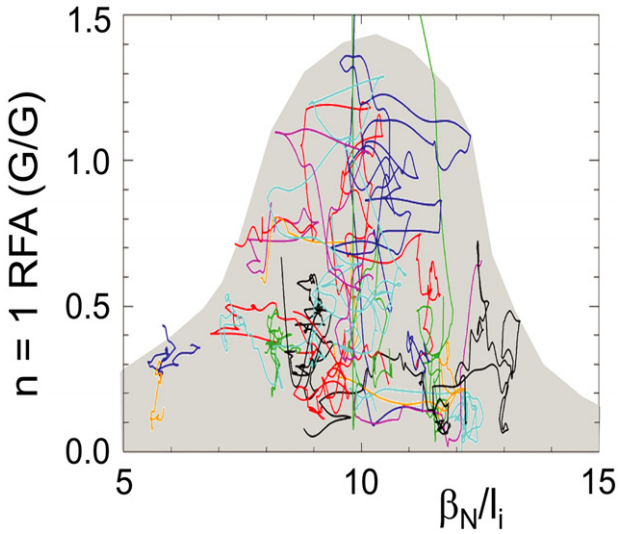

Figure 16. $n = 1$ RFA versus β_N/l_i during high β discharges using active MHD spectroscopy, indicating improved stability at high β_N/l_i.

in initial low l_i experiments to 14% with this control, but remarkably, the reduced disruption probability was observed mostly in plasmas at high $\beta_N/l_i > 11$. Disruptions occurred more frequently at intermediate values of β_N/l_i. This agrees with active MHD spectroscopy diagnosis, used to determine the proximity to marginal stability [40] (figure 16). The RFA of an applied 40 Hz co-NBI rotating $n = 1$ seed field shows an increase in RFA to a broad peak near $\beta_N/l_i = 10$. This decrease in RWM stability, shown by the increase in RFA, is expected as β_N increases, and has been as reported for DIII-D [73], JET [74], and NSTX [41, 72] at lower β_N values. In contrast, and remarkably, RFA is found to decrease at higher values of β_N/l_i in NSTX, indicating increased mode stability (figure 16). This positive result is presently not thought to be a second stability region for the RWM, but is more likely related to proximity to broad resonances in plasma rotation (e.g. ion precession drift resonance) providing kinetic stabilization of the RWM [33, 35, 38]. Note that for the plasmas shown in figure 16, the RFA shown is an output quantity, and is not limited by plasma energy confinement or other considerations. The figure illustrates two plasmas (RFA amplitudes increase off-scale in the figure) that become unstable and suffer disruptions at intermediate β_N/l_i. This was not observed at higher β_N/l_i in these experiments. In addition, the plasma boundary configuration is not changed in this database, taken from a dedicated experiment. A more thorough discussion of kinetic RWM stabilization, with direct comparison to NSTX experiments, can be found in the references listed above. As has been utilized in NSTX for many years, alteration of the rotation profile in these experiments is achieved at constant NBI power through non-resonant neoclassical toroidal viscosity generated by an applied $n = 3$ field [75].

In addition to dedicated experiments, a large database of disruption rate and disruptivity statistics, spanning 2006–2010 operation, has been analysed more generally [76]. Figure 17 shows disruptivity as a function of β_N and $q^* \equiv \varepsilon\pi a B_T(1+\kappa^2)/\mu_0 I_p$, pressure peaking factor, $F_p \equiv p(0)/\langle p\rangle$, plasma shaping factor, $S \equiv q_{95} I_p/a B_T$, and l_i. The database includes disruptions caused by various phenomena, including global mode destabilization, tearing mode locking, density limit disruptions, and impurity radiation-induced collapses. RWM instability is a significant cause of disruption in this database. Strikingly, and consistent with dedicated stability experiments described above, no clear increase is found in disruptivity at increased β_N and $l_i < 0.8$. Significant increases in disruptivity are found for $q^* < 2.4$, at low plasma shaping, and at high values of F_p, and l_i, each of which are generally expected [77, 78]. Increased S, and decreased F_p typically beneficial for stability, are also shown to yield reduced disruptivity in this analysis.

Neoclassical tearing mode (NTM) marginal island width data show the relative importance of the enhanced stabilizing curvature effect at low aspect ratio, yielding less susceptibility to NTM onset even if the classical tearing stability index is near marginal. Advantages at low aspect ratio are confirmed by both a larger characteristic small island size for stabilization and the presence of a significant stabilizing curvature effect. Both tend to make NTMs harder to excite. The stabilizing curvature effect could maintain NTM stability of an equilibrium which is even classically unstable, i.e., $\Delta' > 0$ [79].

Coherent edge harmonic oscillations at 2–8 kHz with $n = 4$–6, have been reproducibly observed in ELM-free plasmas using various diagnostics including magnetic pickup coils, USXR, Langmuir probes, and reflectometry. These oscillations have little effect on particle or impurity transport, in contrast to EHOs in DIII-D. The possibility of actively driving these oscillations using high-harmonic fast-wave (HHFW) has been investigated using the IPEC code, which indicates that EHOs can be largely amplified if the HHFW configuration is optimized for $n = 4$–6 [80].

4.2. Dual-field component active RWM control and model-based RWM state-space controllers

Two approaches for improved RWM control have been used and studied in NSTX. First, combined use of radial (24) and poloidal field (23) RWM sensors with proportional gain feedback provided control of $n = 1$ modes [40]. Modelled feedback evolution agrees with experiment for radial sensor variations examined (figure 18), and also shows the optimal gain is still a factor of 2.5 greater than the value used in experiments to date. The second approach is a model-based state-space controller [81] using a state derivative feedback algorithm [82] and incorporating currents due to the unstable RWM eigenfunction and those induced in nearby 3D conducting structure by the applied control field and plasma response. Testing this physics is especially important for ITER [83] and high neutron output devices where greater control coil shielding will be needed. Using a number of states equal to, or greater than required by Hankel singular value analysis (7 states here) provides sufficient 3D conducting structure current detail to match experimental sensors. Open-loop comparisons between sensor measurements and the RWM state space control (RWMSC) model showed agreement with a sufficient number of states and improved agreement when the 3D wall model details (e.g. NBI ports) were added (figure 19). Control was demonstrated to sustain long pulse,

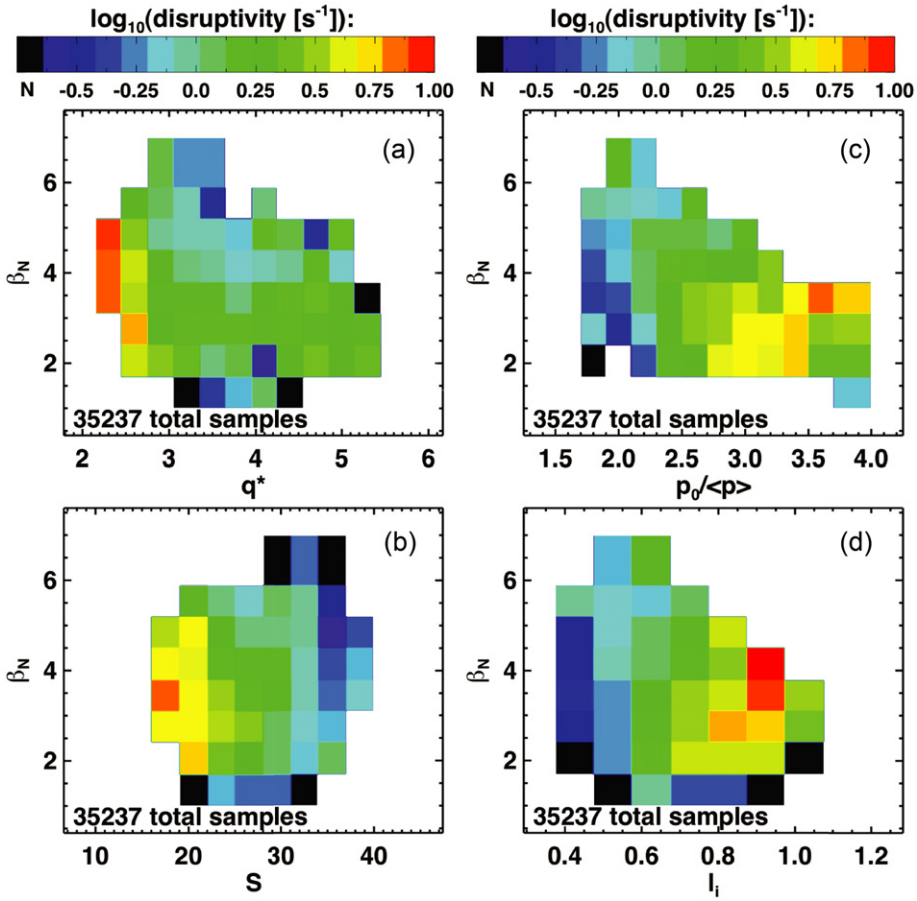

Figure 17. Disruptivity as a function of β_N and (*a*) $q*$, (*b*) shape factor, (*c*) pressure peaking and (*d*) l_i.

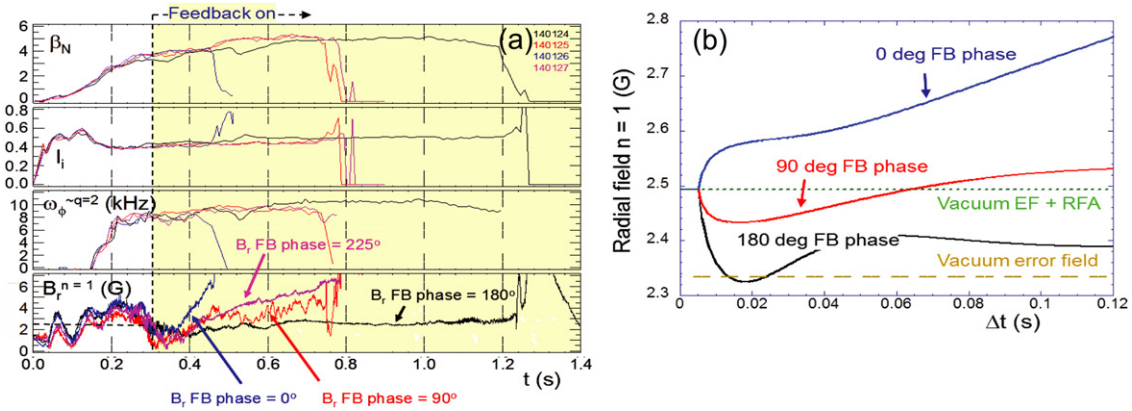

Figure 18. RWM B_R sensor feeback phase variation with combined radial/poloidal field sensor feedback (*a*) experiment, (*b*) theory.

high β_N discharges with $n = 1$ fields applied that normally disrupt the plasma (figure 20). This controller was used for RWM stabilization in long-pulse plasmas (limited by coil heating constraints) reaching $\beta_N = 6.4$, and near maximum $\beta_N/l_i = 13.4$ (shown in figure 15) [40].

4.3. Disruption detectability

An extensive database study has been conducted to determine the detectability of disruptions based on multiple-input criteria [76]. A disruption detection algorithm has been formulated, using as input quantities such as the low frequency $n = 1$ RWM amplitude, neutron emission compared to a computations from a rapidly evaluated slowing-down model, ohmic current drive power compared to simple current drive expectations, and plasma vertical motion (used offline here, but all able to be evaluated in real-time); the algorithm has been tuned to maximize disruption detectability while minimizing false positives or late warnings. Results illustrate that no single diagnostic dominates the detection algorithm; a combination of signals is required. In total, 17 threshold tests are evaluated every 2 ms, and a point value is produced for each test; the

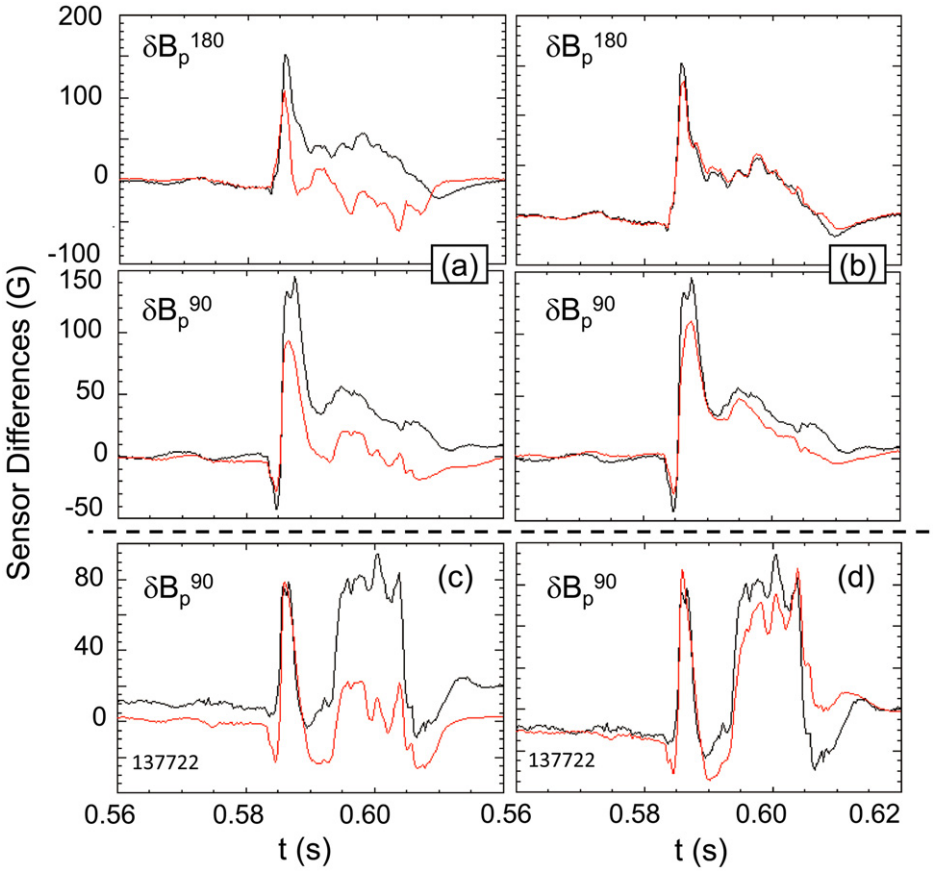

Figure 19. Open-loop comparison of RWM sensor subset (black lines) with RWMSC observer (red lines): (*a*) 2 states, (*b*) 7 states, (*c*) without, and (*d*) with the inclusion of the NBI port (7 states).

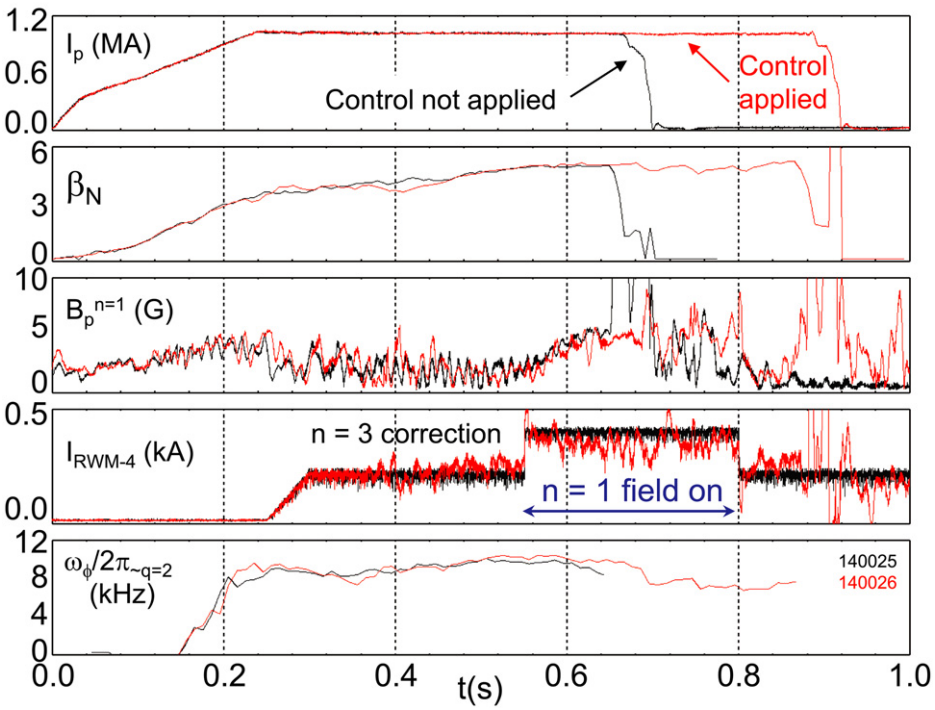

Figure 20. High β_N NSTX plasma utilizing RWM state-space control (red lines) to survive an otherwise disruptive $n = 1$ field perturbation suffered when the control was off (black lines).

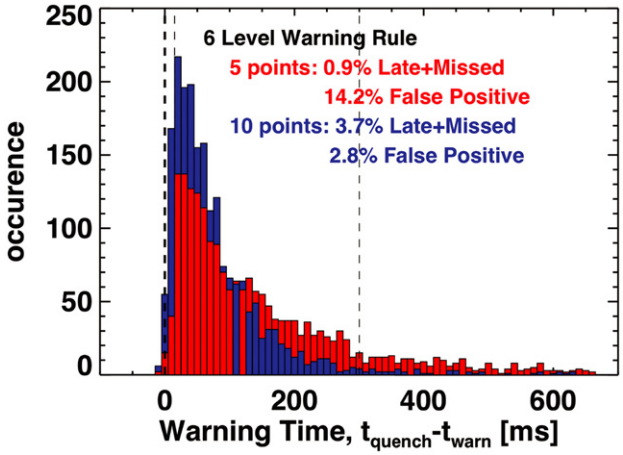

Figure 21. Histogram of warning times computed for 2020 discharges exhibiting disruptions.

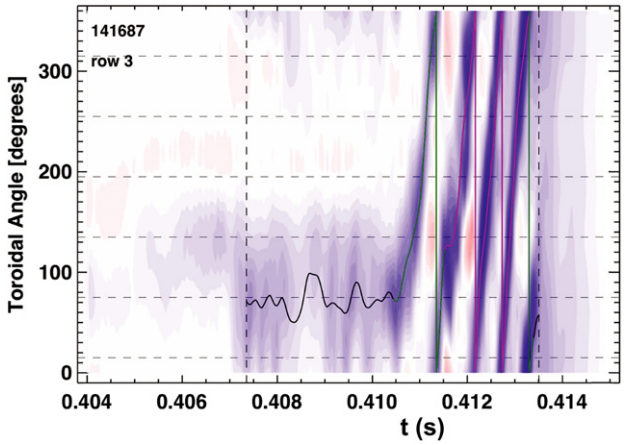

Figure 22. Disruption-induced $n = 1$ halo current dynamics.

sum of the individual point values yields an aggregate point total. A flag noting that a disruption is imminent is set when the aggregate point total is sufficiently large. This approach has shown high success. Figure 21 illustrates a histogram of the warning times that this approach finds for a database of ~2020 discharges with disruptions in the I_P flat-top. When the disruption warning is declared for an aggregate point total of 5 points, the percentage of disruptions detected with at least 10 ms warning is very high (99.1%), but the rate of false positives is also high (14.2%). Here, a false positive is defined as a warning preceding the disruption by more than 300 ms, corresponding to ~5 energy confinement times or 1 current relaxation time. Increasing the threshold on the aggregate point total to 10 results in a disruption detection warning percentage of 96.3%, but significantly reduces the false positive percentage to 2.8%. The majority of false positives are due to near-disruptive events, such as rotating MHD modes that slow the rotation, or lock to the wall, but do not lead to an immediate disruption. The small number of missed warnings found is largely due to locked modes and RWMs that grow more rapidly than the 10 ms warning time required to issue a successful warning. Such a disruption prediction system is planned for use in NSTX-U.

4.4. Halo current characteristics and dynamics

Disruption-induced halo currents [84] are often observed and can have significant toroidal asymmetry. The currents are measured using an array of six shunt tiles mounted on the divertor floor. An $n = 1$ current asymmetry is common and can rotate toroidally (up to 7 transits; 2–3 more common) at 0.5–2 kHz. The number of toroidal transits decreases with increasing halo current magnitude. Contours of halo current magnitude are shown in figure 22 for a downward-going vertical displacement event that limits on the outer divertor plate. The halo currents are first observed to flow at nearly fixed toroidal angle. However, at $t \sim 0.411$ s, the observed toroidally asymmetric halo current begins to rotate. The dominant structure of the halo current is a single, toroidally localized lobe. Typical full width at half maximum for these lobes is 2–4 rad, and the rotation frequency and spatial width can vary rapidly during the disruption. The toroidal rotation of the halo currents can also be non-monotonic, with pauses, and reversals in the toroidal phase propagation [76, 85]. Understanding this rotation is important for future large tokamaks and STs, where dynamic amplification of the halo current mechanical loads can occur if the rotation frequency matches the mechanical resonances of the vacuum chamber or in vessel components [86].

5. Energetic particles, modes and 3D field effects and wave–particle interactions

Fast ions from fusion alpha particles and neutral beam ions are expected to affect a wide range of instabilities in an ST-FNSF, CTF, ITER, and DEMO. Present attention focuses on Alfvénic mode diagnosis and the interaction of the fast-particle population and various MHD modes. Additionally, research has been directed at understanding the mechanism causing significant flow of RF power to the divertor region along field lines in the SOL.

5.1. Fast ion phase space redistribution and effects on low and high frequency MHD

TAE avalanches and associated neutron rate reduction studies, previously restricted to L-mode plasmas, have now been extended to H-mode plasmas with centrally peaked density profiles allowing reflectometer measurements of the mode structure [87]. Prompt, classical fast ion losses computed from the gyro-centre particle-following code ORBIT [88] are negligible and cannot fully account for the observed neutron rate reduction. Instead, the simulations predict the TAE activity to induce fast ion energy scattering, causing a small (3–5%) net decrease in fast ion β. This, and the redistribution of fast ions to regions of lower ion density with these peaked profiles can account for most of the measured decrease in neutron rate. The fast ion energy loss is comparable to the estimated energy lost by Alfvén wave damping during the burst [87].

In addition to Alfvénic modes, low frequency $n = 1$ global kinks cause fast ion redistribution as measured by a fast ion D_α diagnostic. This new observation in turn leads to Alfvénic mode destabilization. The low-frequency modes are consistent

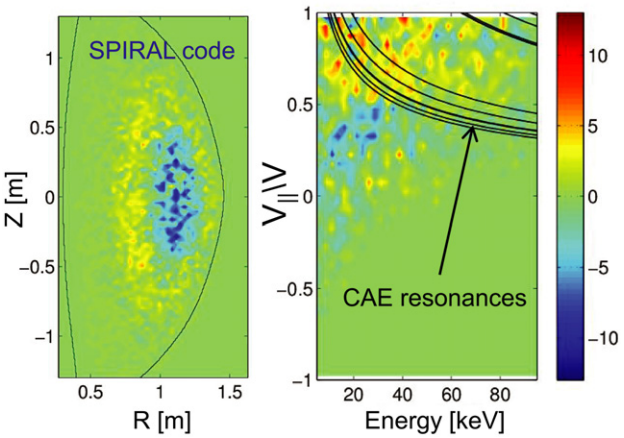

Figure 23. Difference between the fast ion distribution functions simulated with and without a saturated kink mode, in real (left) and velocity (right) space. The loci of potential resonances with CAE modes are indicated by solid curves.

with non-resonant internal kinks [89, 90], destabilized by pressure gradient, whose saturation and nonlinear evolution are modified by fast ions. Full-orbit particle-following code (SPIRAL [91]) calculations have been performed with an ideal kink radial mode structure (PEST code) and validated by soft X-ray data. The simulation indicates that fast ions are redistributed from the core outward, and towards $V_\parallel/V = 1$ where compressional Alfvén eigenmode (CAE) resonances are expected, leading to observed CAE destabilization (figure 23).

Applied $n = 3$ field pulses are shown to alter the stability and behaviour of high frequency instabilities (figure 24) [92]. Beam ions drive persistent bursting/chirping modes between 400–700 kHz. The modes are apparently global Alfven eigenmodes (GAEs) [93] with $n = 7$–9. When the $n = 3$ pulse is applied, the GAE burst frequency triples, the mode amplitude halves, and the frequency sweep extent decreases from 100 to 40 kHz. SPIRAL code analysis, aimed at investigating the modification of fast ion distribution function induced by static external field perturbations, indicates a depletion of the portion of phase space that drives the GAE instabilities. The delay between GAE response and application of the field perturbation can be ascribed to field penetration. This interesting observation may lead to a future control approach for fast-particle driven instabilities. In addition, NSTX-U plasmas operating at up to twice the toroidal field of normal NSTX operation ($B_t = 1$ T) will allow an expanded investigation of the effect of decreasing the ratio of fast-particle velocity to Alfvén velocity on Alfvén eigenmodes. A decrease in this ratio led to a decrease in unstable Alfvénic modes in Globus-M experiments [94].

Stabilizing effects of the energetic particle population have been computed, using the MISK code, to play a significant role in the RWM stability of NSTX plasmas [38]. Extrapolation to ITER Advanced Scenario plasmas shows that the stabilizing effect of alpha particles will be required at expected plasma rotation levels, but ITBs may alleviate the needed α stabilization by strengthening the stabilizing ion precession drift resonance [40].

5.2. Measurement and structure of internal CAE and GAE

Identification of observed high frequency Alfvénic mode activity as GAE, CAE is essential to understanding how they will affect the plasma, as they will have different effects on resonant particle orbits. However, distinguishing between CAEs and GAEs has sometimes proven difficult. For instance, one commonly used indicator [95–97], the polarization of edge magnetic fluctuations, has been shown to be problematic because shear Alfvén eigenmodes such as GAEs can have a strong compressional component in the plasma edge of a ST [98].

Detailed measurements of high frequency AE amplitude and mode structure were obtained in high power NBI-heated H-mode plasmas [99] very similar to those in which high frequency AE activity (identified as GAEs) was shown to correlate with enhanced core electron thermal transport [100]. These measurements extend for the first time into the core H-mode plasma, permitting investigation of the role of the modes in the transport enhancement. The modes are measured using an array of fixed-frequency reflectometers and a toroidally distributed array of magnetic pickup coils (figure 25). The reflectometers operate at frequencies distributed over 30–75 GHz, corresponding to cutoff densities of $(1.1\text{–}6.9) \times 10^{13}$ cm^{-3} when operating with ordinary-mode polarization. The radial structure and amplitude measurements of the modes are obtained using the reflectometer arrays, which measure the phase shift, $\delta\phi$, of the probing millimetre-waves caused by the density fluctuations associated with the modes. For modes with large radial extent, this is dominated by displacement of the cutoff locations. The figure shows $\xi = \delta\phi/2k_0$ (k_0 is the vacuum millimetre-wave wavenumber), which approximates the displacement of the cutoff location. Mode identification is made by comparing frequency and toroidal mode numbers with local Alfvén dispersion relations. The observed CAEs have higher frequencies ($f >\sim 600$ kHz) and smaller toroidal mode numbers ($|n| \leqslant 5$) than the GAEs ($f <\sim 600$ kHz, $n = -6$ to -8) and are strongly core localized. GAEs also peak towards the plasma centre, but have much broader radial extent. Recent simulations using the HYM code show unstable sub-MHz, low-n CAEs in these H-mode plasmas [98].

5.3. RF power flow in the SOL

HHFW heating and current-drive efficiencies can be significantly lowered by interactions of the HHFW power with the edge plasma in the SOL [101, 102]. One manifestation of these edge interactions is bright streaks emanating from the antenna and reaching to both the upper and lower divertor regions where bright spirals are produced (figure 26(*a*)). The location of the spiral trajectories in the divertor regions is consistent with the hypothesis that the lost HHFW power flows through the SOL to the divertor regions along magnetic field lines that pass in front of the antenna [103]. This conclusion is reached by tracing the field lines to the points where they strike the divertor using the SPIRAL code [91] and comparing these strike points with experimental measurements such as divertor infrared (IR) camera data [104]. These observations imply that HHFW power is lost along field lines across the entire width of the SOL, i.e., all field lines between the antenna

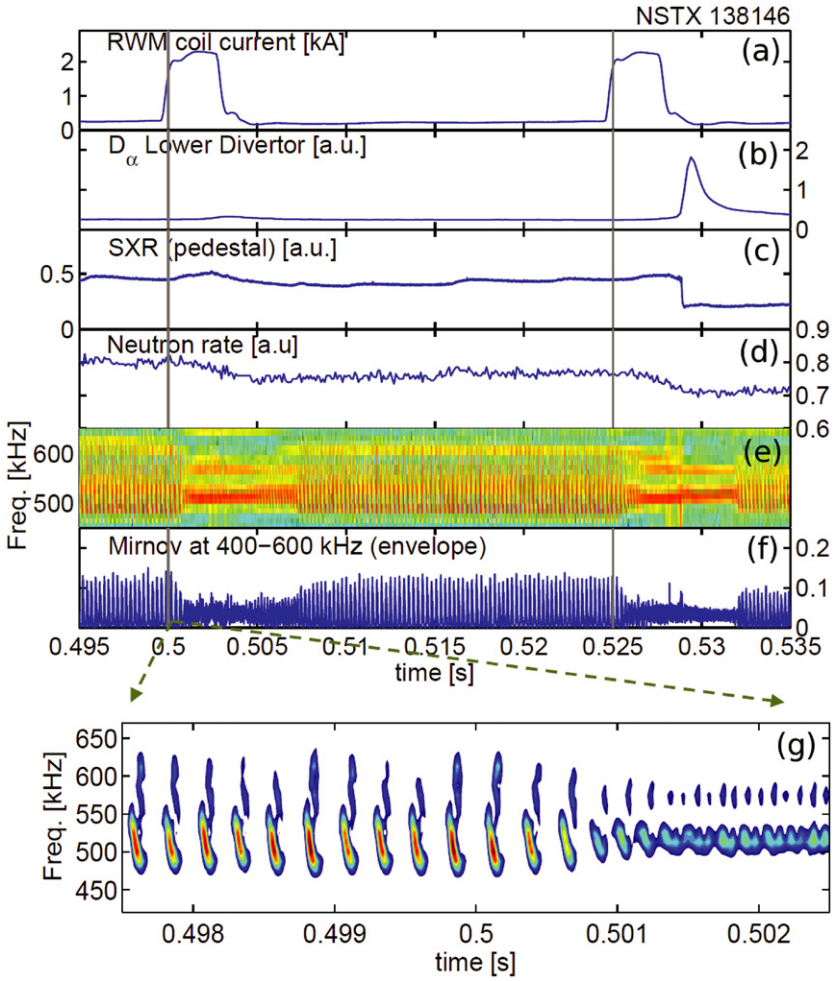

Figure 24. Modification of GAE activity during applied $n = 3$ fields: (*a*) RWM coil current, (*b*) D_α and (*c*) SXR emission, (*d*) measured neutron rate. (*e*) frequency spectrum and (*f*) rms signal amplitude of magnetic fluctuations from Mirnov coils. (*g*) Detail of frequency evolution around $t \sim 0.5$ s.

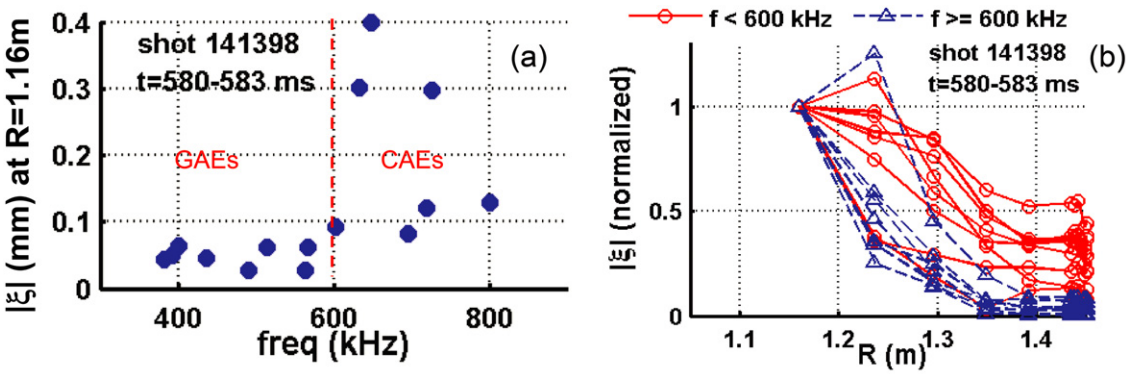

Figure 25. (*a*) Effective radial displacement ($|\xi|$) of GAE and CAE modes at $R = 1.16$ m; and, (*b*) $|\xi|$ vs. R, normalized by $|\xi|$ at $R = 1.16$ m in H-mode plasma.

and the last closed flux surface (LCFS), and not solely to field lines connected to antenna components. Thus, these losses to the divertor region are distinct from, and in addition to RF sheath losses on antenna components [105]. Indeed, when the HHFW-produced lower divertor heat flux is mapped back to the midplane in front of the antenna using field-line mapping (figure 26(*b*)), the profile of the lost power is relatively large close to both the antenna and near the LCFS. The mapping procedure used in figure 26(*b*) incorporates poloidal flux expansion and projection effects, and the points correspond to the different passes of the spiral across the toroidal position of the diagnostic. The gaps in-between points indicate radial locations where the spiral lands away from the toroidal position of the IR camera and is therefore not measured. There is a low heat flux associated with the second pass of the spiral [106]. It is hypothesized that these losses

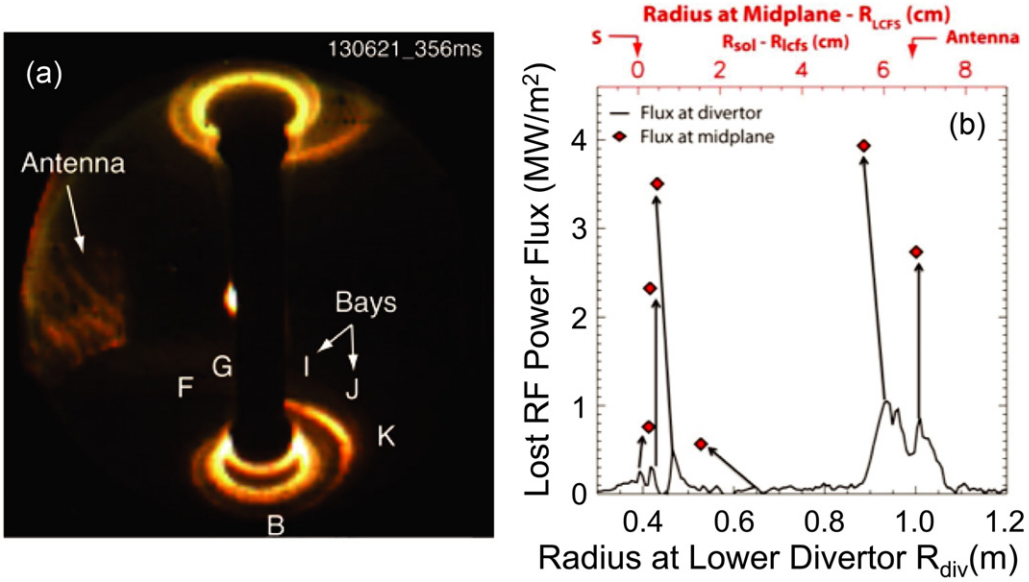

Figure 26. (*a*) Visible camera image of HHFW power interaction with edge plasma and resulting heat spirals on upper and lower divertor, (*b*) HHFW-produced heat flux to the lower divertor at the position of the IR camera (bay I) (line), and corresponding power flux lost at the device midplane (points).

are due to fast-wave propagation in the SOL [102] and that the profile of lost HHFW power is due to a radial standing wave caused by partial reflections off the steep pedestal gradients. Experiments on NSTX-U will aim to confirm or deny the presence of RF fields in the divertor region. It is important to determine the mechanism underlying these field-aligned losses to the divertor, as this mechanism must be included in RF codes that include the SOL [107] to accurately predict fast-wave heating performance in future devices.

6. Heat flux mitigation and L–H power threshold: effects of boundary configuration

6.1. Radiative snowflake divertor

The standard radiative divertor solution may be insufficient to handle the significantly higher heat fluxes expected in an FNSF, or DEMO. The snowflake divertor configuration [108] enables edge magnetic shear, divertor plasma-wetted area, connection length and divertor volumetric losses to increase beyond those of the standard divertor configuration [10, 109]. This configuration, enhanced by radiative detachment, exhibits a significant reduction in both steady-state and ELM divertor heat fluxes (a significant concern for ITER [110, 111]), high core plasma confinement with reduced core impurities, and stable operation. The plasma-wetted area is increased up to 200%, X-point connection length 50–100%, and the divertor volume up to 60%. The formation of a snowflake-minus configuration was quickly followed by a partial detachment of the strike point. The peak divertor heat flux decreased from 7 to less than 1 MW m^{-2} [112] between ELMs. Core H-mode confinement with $\tau_E \sim$ 50–60 ms, plasma stored energy of 200–250 kJ and H98(y, 2) $\sim$ 1 was maintained, and core and edge carbon concentration was reduced by up to 50%. During snowflake configuration operation, type-I ELMs stabilized by pedestal changes linked to the use of lithium (section 3.1)

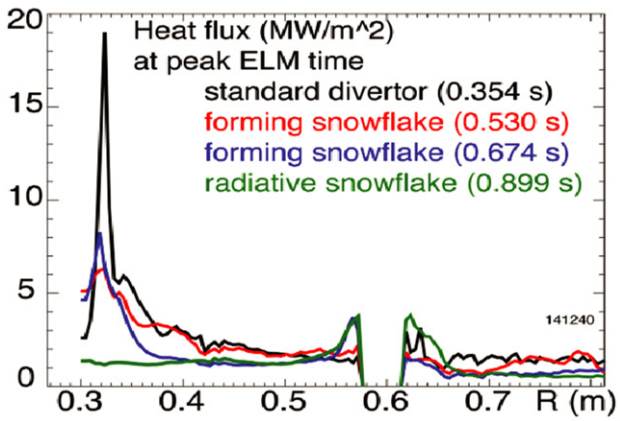

Figure 27. Outer divertor heat flux profiles for standard and snowflake divertors during type-I ELMs. The lack of data near $R = 0.6$ m is due to the gap between the inner and outer parts of the vessel. The primary outer strike point is located at 0.3–0.32 m.

re-appeared [113]; however, heat fluxes from these type-I ELMs ($\Delta W_{\rm plasma}/W_{\rm plasma}$ = 7–10%) were significantly dissipated (figure 27) in the strike point region, reduced from 19 to 1 MW m^{-2}. The increase of the temperature and heat flux towards the gap between the inner and outer parts of the vacuum vessel shown in the figure is only seen at peak ELM times, and no such increase is observed between ELMs. Peak target temperatures, measured by fast IR thermography during ELMs in this region reached 1000–1200 °C in the standard divertor and only 300–500 °C in the snowflake configuration. This is consistent with both the lower surface temperature rise due to the longer convective heat deposition time due to the longer L_x in the snowflake divertor, and the convective heat redistribution mechanism in the null-point region proposed theoretically [114]. The snowflake divertor configuration was maintained during ELMs, however, the radial extent of the partially detached zone was reduced. The snowflake divertor

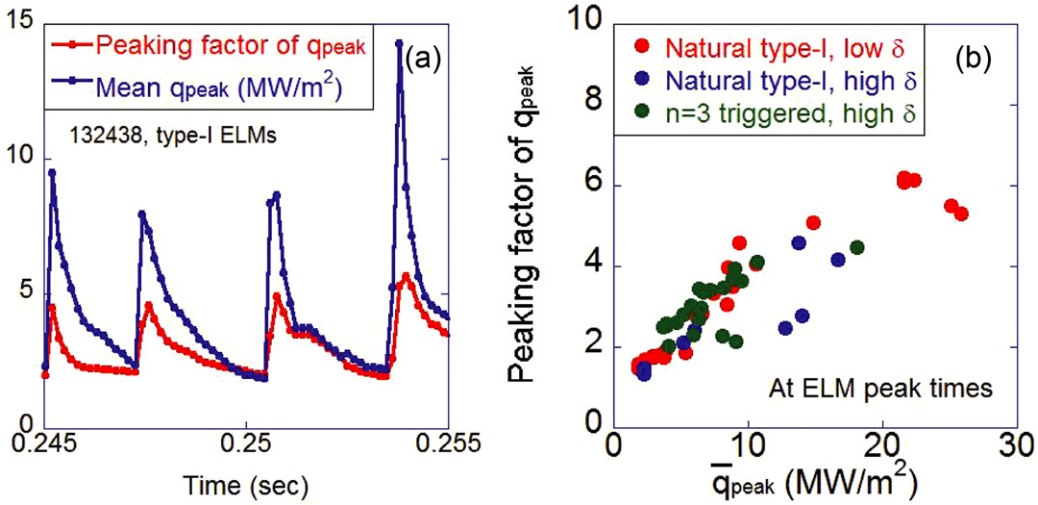

Figure 28. (*a*) Evolution of measured mean peak heat flux and toroidal peaking factor during type-I ELMs. (*b*) Toroidal peaking factor of q_{peak} during ELM activity occurring naturally, or triggered by 3D applied field pulses.

configuration is a leading candidate for divertor heat flux mitigation in NSTX-U. In this case, two up-down symmetric sets of four divertor coils will be used to test snowflake divertors for handling the projected steady-state peak divertor heat fluxes of 20–30 MW m^{-2} for a standard divertor [8] in 2 MA discharges up to 5 s long with up to 12 MW NBI heating.

6.2. *Effects of non-axisymmetry and 3D fields*

Application of 3D fields has been used for several positive applications on NSTX, including MHD mode control, including ELMs, and to control plasma rotation [75, 115, 116]. Expanded use of 3D fields in these and other roles are planned for NSTX-U. Therefore, 3D field applications and heat flux reduction techniques must be compatible. A toroidal asymmetry of heat deposition is observed on NSTX during ELMs, or by application of 3D fields. These studies are known to each be of general interest, with past research on ASDEX Upgrade [117], COMPASS-D [118] and DIIII-D [119–121] that has direct application to ITER. In the present work, the asymmetry in the toroidal distribution of peak heat flux, q_{peak}, quantified by a toroidal peaking factor, and the heat flux width, λ_q, become largest at the peak of the ELM heat flux [122]. Data for this study are taken from an IR camera located at one toroidal position that covers a toroidal extent of 20°–50° with a sampling rate in the range 1.6–6.3 kHz and a spatial resolution of about 0.6 cm. The 2D heat flux profiles are quantitatively analysed using a newly implemented 3D heat conduction code [123], and the toroidal asymmetry in heat flux is estimated by a single figure of merit (toroidal peaking factor of peak heat flux defined as the ratio max(q_{peak})/mean(q_{peak}) from the toroidal array of measurements) to represent the entire 2D plane observed by the IR camera. The toroidal peaking factor of the peak heat flux during the ELM cycle is shown in figure 28(*a*). This is a serious concern for first-wall tile design and cooling requirements, which are usually based on 2D axisymmetric calculations. Present data indicates that the toroidal peaking factor of q_{peak} does not depend on whether the ELM activity is naturally occurring, or is instead triggered by applied $n = 3$ fields [116] (figure 28(*b*)).

While the asymmetry caused by the applied 3D fields can re-attach a partially detached radiative divertor plasma due to an increase in pedestal T_e, additional gas puffing can restore detachment [124]. Applied 3D field pulses with amplitudes below ELM triggering level show increased D_α intensity, indicating increased particle transport. The EMC3-EIRENE code package [125, 126] has been used to model the divertor fluxes and flux patterns in discharges with applied $n = 3$ applied fields. The code solves the 3D plasma fluid equations with ad-hoc radial transport coefficients (EMC3) and kinetic neutral recycling and transport (EIRENE) in general 3D magnetic fields. Using the superposition of axisymmetric equilibrium fields with vacuum perturbation fields, i.e., with no screening due to plasma currents, and a choice of cross-field coefficients used in previous 2D modelling [127], the measured trends and splitting in the divertor heat flux and D_α are qualitatively reproduced [128].

6.3. *L–H power threshold dependence on X-point position and effects of lithium*

The heating power required for accessing H-mode decreases as the triangularity decreases (larger X-point radius) and divertor recycling decreases via lithium deposition [129, 130]. The open divertor and ability to pump both strike points with lithium deposition regardless of the strike point location on NSTX provides an opportunity to decouple the dependence of the L-to-H mode power threshold, P_{LH}, on changes to the X-point location and the divertor pumping. The P_{LH} decreased 30% as the X-point radius was increased to create a low-triangularity shape (figure 29(*a*)). Lithium wall conditioning was kept nearly constant during these experiments. The edge ion and electron temperatures at the time of the L–H transition appear to scale with triangularity, but were nearly constant for each shape despite large changes in the divertor recycling and core heating power. The L-mode gas fuelling rate is chosen to maintain a constant edge density or constant line-averaged density. In both shapes, increased divertor pumping due to lithium deposition reduced P_{LH} by 17% when matching line-averaged density, and by 50% when matching edge density.

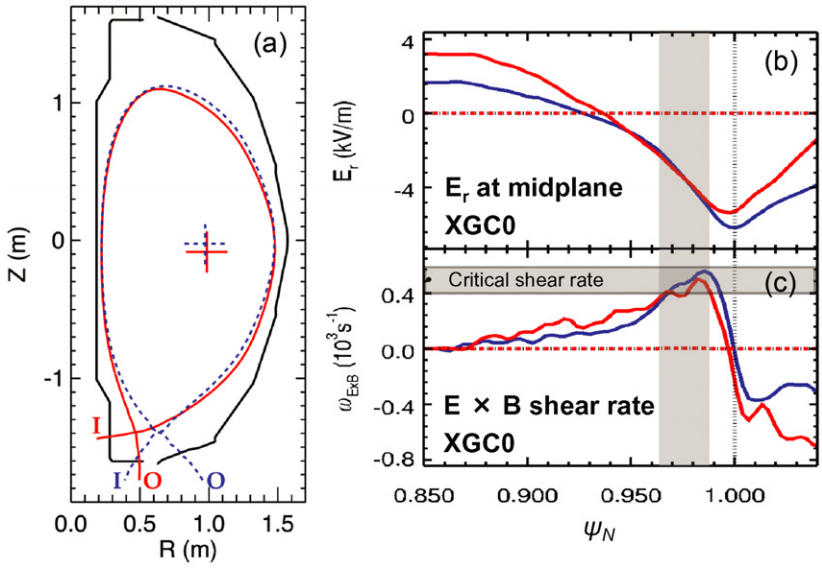

Figure 29. (*a*) Alteration of X-point position in H-mode power threshold experiment, and corresponding (*b*) midplane E_r and (*c*) $E \times B$ shearing rate profiles versus normalized poloidal flux from XGC0 simulations. The high-triangularity shape (solid red line) requires 30% more core heating to achieve the larger edge T_i necessary for generating a similar E_r and $E \times B$ shear as a low-triangularity shape (dashed blue line).

Note that past experiments have characterized the dependence of P_{LH} on density and did not find a minimum in the P_{LH} versus n_e curve for deuterium and helium [130]. This suggests that NSTX operates within the high-density branch of the P_{LH} versus n_e curve with a nearly linear relationship between P_{LH} and density.

Full-f kinetic neoclassical XGC0 simulations [131] indicate the P_{LH} versus X-point major radial position, R_X, scaling can be attributed to changes in the $E \times B$ shear driven by an ion orbit loss hole, or X-transport [132]. The $E \times B$ flow shear driven by X-transport increases with both R_X and ion temperature, T_i. Therefore, achieving a critical level of $E \times B$ flow shear should require a smaller T_i as R_X increases. The XGC0 modelling indicates that the high-triangularity shape on NSTX requires 30% larger ion heating and edge T_i to achieve the same level of $E_r \times B$ flow shear in L-mode (figure 29), which is in quantitative agreement with experiment. XGC0 calculations have also illustrated the impact of the poloidal distribution of neutral fuelling on the edge flows [5]. When the neutral fuelling source is changed from being localized to the divertor to distributed throughout the SOL (indicative of a lower recycling divertor with increased fuelling from injected gas), the ion heating power needed to maintain the same edge T_i and $E_r \times B$ flow shear decreased by 20%, which is also in qualitative agreement with E_r computed from TRANSP analysis using experimental profile data.

7. Non-inductive current results and operational scenarios for NSTX-U

7.1. Co-axial helicity injection

Transient co-axial helicity injection (CHI) has generated 300 kA peak toroidal current and 200 kA on closed flux surfaces without the use of the central solenoid. When induction from the solenoid was added to CHI start-up, plasmas that ramped to 1 MA required 35% less inductive flux. These discharges have high elongation ~2.6, low plasma density and $l_i \sim 0.35$ desirable for achieving advanced scenarios [133]. Full discharge simulations using the TSC code, including CHI and subsequent current ramp-up using neutral beams, show favourable scaling of the CHI start-up process with increasing toroidal field, which will be doubled in NSTX-U. This analysis predicts at least a doubling of the closed flux current for NSTX-U [134].

7.2. Non-inductive current by NBI and RF

H-mode plasmas with $I_p = 0.3$ MA, $B_T = 0.55$ T, and 1.4 MW of 30 MHz HHFW power with current drive phasing have reached a NICF of 70%, to as high as 100% for brief periods of operation (much shorter than the resistive skin time) as computed by TRANSP-TORIC analysis (figure 30). The quoted range in NICF comes primarily from the fluctuation in the bootstrap current modelling as the discharge evolves. With an estimated RF coupling efficiency of 60%, direct RF-driven current is 60–70 kA. The computed bootstrap current varies from 100 to 230 kA. The current generated directly by HHFW power was generated inside a normalized minor radius ~0.2, and 75% of the non-inductive current was generated inside a normalized minor radius ~0.4 [135]. Over the entire range of NBI heated plasmas, up to 65% NICF was experimentally reached (computed by TRANSP), peaking at plasma current value of $I_p = 0.7$ MA (figure 31). The wide range of I_p for projected 100% NICF operation in NSTX-U based on these plasmas is also shown [136].

7.3. Fully non-inductive scenarios for NSTX-U

Significant progress has been made on the present hardware upgrade of NSTX. A major milestone for NSTX-U (and a decades-long goal for tokamak operation in general) is routine operation at 100% non-inductive fraction. Such operation is expected to bring new challenges and opportunities

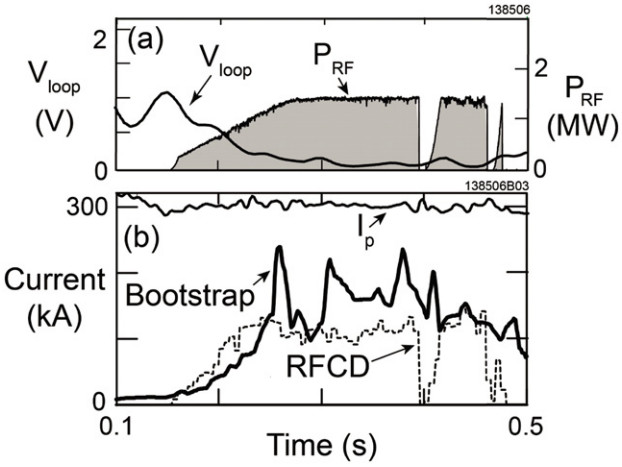

Figure 30. (*a*) Time evolution of the loop voltage and RF power for an $I_p = 0.3$ MA, HHFW-only H-mode plasma. (*b*) Time evolution of the plasma current, and bootstrap and direct RF-driven current predicted by TRANSP-TORIC.

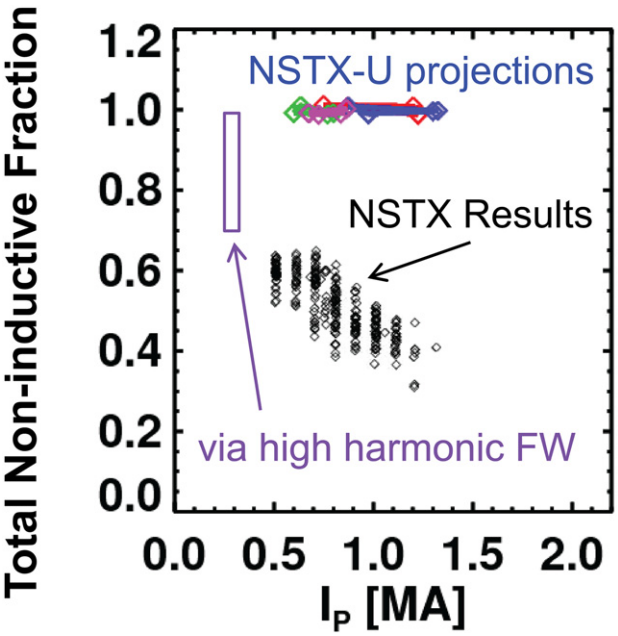

Figure 31. NICF versus I_p in NBI and HHFW H-mode plasmas.

for understanding tokamak transport and stability. Routine operation of NSTX at high NICF allows confident projection to potential 100% non-inductive operational scenarios for NSTX-U. Experimental scenario development in NSTX has already accessed the aspect ratio (up to 1.73) and boundary shaping (elongation greater than 2.9) planned for NSTX-U [136, 137]. Predictive TRANSP calculations have been conducted [136] using a range of NSTX profiles shapes and confinement level assumptions, and project 100% NIC fraction over a wide range of I_p from 0.6–1.35 MA, capability for an order of magnitude collisionality variation, and a factor of 4 collisionality reduction compared to NSTX for fully relaxed plasmas with $q_{min} > 1$. Profile shapes with both the narrowest and broadest H-mode thermal pressure profiles typically found in NSTX were used in these predictive calculations; furthermore, both the standard ITER-98y,2

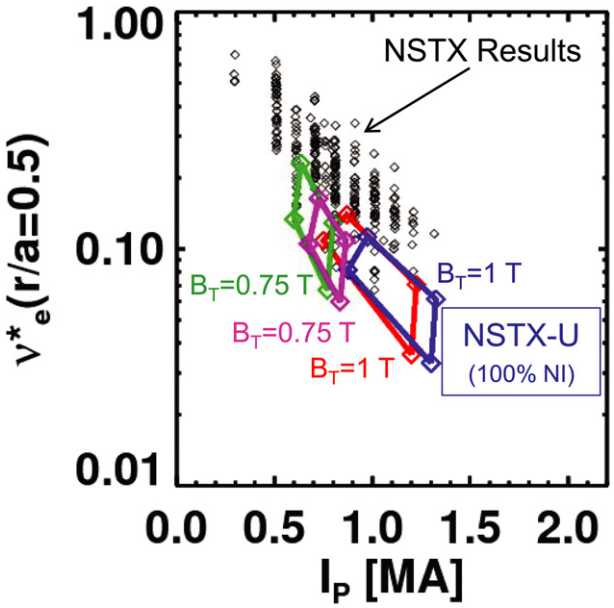

Figure 32. Projected (I_p, ν^*_e) operational space in NSTX-U with 100% NICF. NSTX experiments have produced up to 65% NICF.

and an ST specific thermal confinement scaling expression [138] were used. These two profile assumptions and two confinement assumptions yield a set of four operating points for a given set of engineering parameters such as the toroidal field, plasma density, boundary shape, and heating power. Figure 32 shows the ranges defined by these assumptions, superimposed on the NSTX operating space, in a plot of mid-radius electron collisionality versus plasma current. The NSTX data are from the same discharges as in figure 31, and thus have non-inductive fractions in the range of 30–65%. The NSTX-U projections, however, are for 100% non-inductive scenarios (at a density corresponding to a Greenwald density fraction, $f_{GW} = 0.7$). This figure shows that as the field is increased from $B_T = 0.75$ T to $B_T = 1.0$ T, the projected non-inductive operating space moves from 500–700 kA, up to 900–1350 kA, where the ranges again account for different profile and confinement assumptions. A key observation is that these scenarios are projected to have simultaneously higher non-inductive fraction and lower collisionality than the NSTX cases, and will represent a major step forward in ST development when achieved.

8. Summary of results and discussion of physics for NSTX-U and future devices

In over a decade of research, NSTX has been used to investigate high beta plasma operation with plasma current at the 1 MA level. The present paper surveyed the physics research conducted during the final operation of the device preceding a significant device upgrade, with operation of the new NSTX-U device planned to start during the last quarter of 2014. The research targets predictive physics understanding needed to extrapolate plasma transport, stability, power handling, non-inductive sustainment, and advanced control techniques confidently towards the goal of a steady-state Fusion Nuclear Science Facility and Component Test Facility. The research

also directly supports ITER, with the unique advantage of levering the low device aspect ratio (down to 1.3) and high beta capabilities to challenge tokamak theory and experimental experience at higher aspect ratio. Over the years of NSTX operation, this advantage has led to physics insights that have altered the projection of physics results to future devices. High beta plasmas have been produced, reaching twice the level of β_N/l_i of the $n = 1$ no-wall ideal stability limit and have subsequently focused on maintaining this high β_N condition indefinitely through passive and active control techniques. A major focus of research that bridges directly to NSTX-U is the effect of collisionality on plasma transport, stability, and rotation control. These studies may influence the design of future devices, such as an ST-FNSF/CTF significantly, as such a device will operate at collisionalities of at least an order of magnitude less than the operating range of NSTX. A scaling of $B_T\tau_E$ appropriate for varied wall conditions exhibits a strong increase with decreasing electron collisionality. Nonlinear microtearing simulations match experimental electron diffusivity quantitatively and predict reduced electron heat transport at lower collisionality. Resistive wall mode growth rates are theoretically and experimentally found to decrease with decreasing ion collisionality when the plasma rotation profile is near broad kinetic stabilizing resonances (e.g. in NSTX, with the ion procession drift frequency). Plasma characteristics change nearly continuously with increasing Li evaporation on plasma facing components between discharges with no Li accumulation in the core plasma. ELMs are stabilized by Li application by changing the density profile. When ELMing, plasmas reach the peeling mode limit, with closer agreement found using XGC0 calculations of the bootstrap current that is more accurate in the higher collisionality edge region. A pedestal width scaling is found that is close to linear in β_p^{ped}, which is stronger than the usual $(\beta_p^{ped})^{0.5}$ scaling found in tokamaks. BES measured turbulence in the steep gradient region of the pedestal is most consistent with turbulence caused by trapped electron instabilities. At the top of the pedestal, the measured and computed spatial turbulence structure exhibits ion-scale microturbulence, compatible with ion temperature gradient modes or kinetic ballooning modes.

Plasmas have reached high values of β_N and β_N/l_i appropriate for ST-FNSF/CTF, and ST-Pilot plant operation. Attention in research has been placed on maintaining these conditions, and understanding the underlying physics. Active $n = 1$ feedback control yielded a significant reduction in disruption probability at high β_N/l_i in controlled experiments. Surprisingly, the disruption probability in these experiments decreased at the highest $\beta_N/l_i > 10$, and increased significantly at lower β_N values closer to the $n = 1$ no-wall ideal stability limit. This result was independently confirmed by experiments utilizing low frequency MHD spectroscopy, which showed RWM stability decreasing up to $\beta_N/l_i = 10$, and then increasing as β_N/l_i was further increased. This highly positive result shows that operation at higher β_N and with higher bootstrap current fraction can be *more* favourable for future tokamak operation. This result is consistent with a theoretical model of kinetic RWM stabilization shown to quantitatively agree with RWM marginal stability in NSTX plasmas. An extensive study of plasma disruptivity conducted using NSTX plasmas created since 2006 shows essentially no dependence of disruptivity versus β_N at low l_i values less than 0.8. NTM marginal island width data show the relative importance of the enhanced stabilizing curvature effect at low aspect ratio, yielding less susceptibility to NTM onset even if the classical tearing stability index is near marginal. Coherent edge harmonic oscillations have been reproducibly observed in ELM-free plasmas, however, these oscillations to date have little effect on particle or impurity transport, in contrast to EHOs in DIII-D. Dual-field component active $n = 1$ RWM control was used to produce the reduced disruption probability in high β_N plasmas. Control of the added radial field perturbation was clear, with feedback phase and RFA dynamics in experiment matching theoretical simulations. An RWM state-space controller, using a state derivative feedback algorithm and currents from an unstable RWM eigenfunction and nearby 3D conducting structure was used in plasmas reaching $\beta_N = 6.4$, and near maximum $\beta_N/l_i = 13.4$. A highly-successful disruption detection algorithm has been devised utilizing multiple threshold tests and applied to the existing NSTX database. Depending on the criteria used in the detection algorithm, the percentage of disruptions predicted with 10 ms warning is found to be very high, ranging from 96.3–99.1%, with the percentage of false positives for these values being 2.8% and 14.2% respectively. Halo currents during disruptions have significant toroidal asymmetry, can rotate many toroidal transits, and the dynamics are complex, including reversals in the change of the toroidal phase.

Fast-ions from fusion alpha particles and neutral beam ions are expected to affect a wide range of instabilities. Computed prompt fast ion losses modelling TAE avalanches in H-mode plasmas are negligible and cannot explain the observed neutron rate reduction in experiment. Instead, simulations predict the TAE activity to cause fast ion energy scattering, decreasing in fast ion β, and redistribution of fast ions to regions of lower density, which can account for the measured decrease in neutron rate observed. Low frequency global kinks have been shown to cause fast ion distribution, which in turn have affected CAE stability. This new result is a reversal of the usual finding of AE activity causing fast-particle redistribution, causing alteration of lower frequency MHD mode activity, such as RWMs. The application of 3D fields with dominant $n = 3$ has been shown to affect GAE stability, indicating that the modes might be controlled in the future using closed-loop feedback. Alfvén eigenmodes have been measured in the plasma core in H-mode plasmas, and the frequency and mode displacements have been characterized. HHFW power is shown to couple to field lines across the entire width of the SOL, not solely to field lines connected to antenna components, which shows the importance of the inclusion of this phenomenon in designing future RF systems.

The snowflake divertor configuration has demonstrated significant reduction of divertor heat flux in both steady-state conditions, and during ELMs. Peaks values of 19 MW m^{-2} to about 1 MW m^{-2} were attained when the snowflake configuration was combined with radiative detachment. This configuration is planned to handle the high heat fluxes (20–30 MW m^{-2}) projected for high current NSTX-U plasmas. Toroidal asymmetry of heat deposition to the first wall is observed during ELMs, or by application of 3D fields. This

is a serious concern for first-wall tile design and cooling requirements. The L-to-H-mode power threshold is found to depend on X-point radial position. Full-f kinetic neoclassical simulations indicate that this observation can be attributed to changes in the $E \times B$ shear driven by an ion orbit loss hole, or X-transport.

A significant milestone for NSTX-U is routine operation with 100% non-inductive current for pulse durations of several current redistribution times. Routine operation in this manner has been a decade-long goal for advanced tokamak operation in general. Present NSTX operation has reached 65% non-inductive fraction at $I_p = 0.7$ MA, and between 70% and 100% NICF at $I_p = 0.3$ MA using HHFW current drive. This allows confident extrapolation to NSTX-U scenarios using the predictive TRANSP code, which show that 100% NICF operation will be possible over a broad range of NSTX-U operation with $0.6 < I_p(\text{MA}) < 1.35$. Scenario development experiments in NSTX have already accessed aspect ratio (up to 1.73) and boundary shaping (elongation greater than 2.9) planned for NSTX-U.

Significant progress has been made in the construction of NSTX-U, that will allow research at twice the plasma current (up to 2 MA), toroidal field (up to 1 T), and NBI power (up to 12 MW) of the NSTX device. Additionally, the added NBI power will be deposited more tangentially, enabling a significantly broader deposition of heat, current drive, and momentum input to expand present physics research, the majority of which is dependent on these profiles. New and unique profile control possibilities to support this research will be enabled by these hardware upgrades, including current profile control of broad current profiles, and the use of both NBI and non-resonant neoclassical toroidal viscosity (NTV) magnetic braking from a 3D applied field as actuators for rotation profile control. Progress on the major new components of the upgrade includes the final placement and positioning of the second neutral beam, and the fabrication and assembly of the centre post toroidal field conductors.

Acknowledgments

This research was funded by the United States Department of Energy under contract DE-AC02-09CH11466, and additional contracts and grants supporting the collaborative team.

References

[1] Ono M. *et al* 2000 *Nucl. Fusion* **40** 557
[2] Peng Y.K.-M., Canik J.M. and Diem S.J. 2011 *Fusion Sci. Technol.* **60** 441
[3] Peng Y.K.-M. *et al* 2009 *Fusion Sci. Technol.* **56** 957
[4] Peng Y.K.-M *et al* 2005 *Plasma Phys. Control. Fusion* **47** B263
[5] Menard J.E. *et al* 2011 *Nucl. Fusion* **51** 103014
[6] Wilson H.R., Ahn J. and Akers R. 2004 *Nucl. Fusion* **44** 917
[7] ITER Physics Basis Editors *et al* 1999 *Nucl. Fusion* **39** 2137
[8] Menard J.E. *et al* 2012 *Nucl. Fusion* **52** 083015
[9] Bell M.G. *et al* 2009 *Plasma Phys. Control. Fusion* **51** 124054
[10] Soukhanovskii V.A. *et al* 2012 *Phys. Plasmas* **19** 082504
[11] Ding S. *et al* 2010 *Plasma Phys. Control. Fusion* **52** 015001
[12] Kaye S.M. *et al* 2013 *Nucl. Fusion* **53** 063005
[13] Valovic M. *et al* 2009 *Nucl. Fusion* **49** 075016
[14] Valovic M. *et al* 2011 *Nucl. Fusion* **51** 073045
[15] Guttenfelder W. *et al* 2013 *Nucl. Fusion* **53** 093022
[16] Guttenfelder W. *et al* 2012 *Phys. Plasmas* **19** 022506
[17] Candy J. and Waltz R.E. 2003 *J. Comput. Phys.* **186** 545
[18] Candy J. and Belli E. 2010 *General Atomics Technical Report* No GA-A26818
[19] Sabbagh S.A. *et al* 2001 *Nucl. Fusion* **41** 1601
[20] Guttenfelder W. *et al* 2011 *Phys. Rev. Lett.* **106** 155004
[21] Wang E. *et al* 2011 *Phys. Plasmas* **18** 056111
[22] Guttenfelder W. *et al* 2012 *Phys. Plasmas* **19** 056119
[23] Doerk H., Jenko F., Pueschel M.J. and Hatch D.R. 2011 *Phys. Rev. Lett.* **102** 155003
[24] Doerk H. *et al* 2012 *Phys. Plasmas* **19** 055907
[25] Ren Y. *et al* 2011 *Phys. Rev. Lett.* **106** 165005
[26] Ren Y. *et al* 2012 *Phys. Plasmas* **19** 056125
[27] Ren Y. *et al* 2013 *Nucl. Fusion* **53** 083007
[28] Yuh H. *et al* 2011 *Phys. Rev. Lett.* **106** 055003
[29] Peterson J.L. *et al* 2012 *Phys. Plasmas* **19** 056120
[30] Smith D.R. *et al* 2008 *Rev. Sci. Instrum.* **79** 123501
[31] Kaye S.M. *et al* 2007 *Nucl. Fusion* **47** 499
[32] Bondeson A. and Ward D. 1994 *Phys. Rev. Lett.* **72** 2709
[33] Hu B. and Betti R. 2004 *Phys. Rev. Lett.* **93** 105002
[34] Sabbagh S.A., Berkery J.W. and Bell R.E. 2010 *Nucl. Fusion* **50** 025020
[35] Liu Y. *et al* 2008 *Phys. Plasmas* **15** 112503
[36] Berkery J.W. *et al* 2010 *Phys. Rev. Lett.* **104** 035003
[37] Berkery J.W. *et al* 2011 *Phys. Rev. Lett.* **106** 075004
[38] Berkery J.W. *et al* 2010 *Phys. Plasmas* **17** 082504
[39] Reimerdes H. *et al* 2004 *Phys. Rev. Lett.* **93** 135002
[40] Berkery J.W. *et al* 2012 *Proc. 24th Int. Conf. on Fusion Energy 2012 (San Diego, CA, 2012)* (Vienna: IAEA) paper EX/P8-07 (www-naweb.iaea.org/napc/physics/FEC/FEC2012/index.htm)
[41] Sontag A.C., Sabbagh S.A. and Zhu W. 2007 *Nucl. Fusion* **47** 1005
[42] Maingi R. *et al* 2011 *Phys. Rev. Lett.* **107** 145004
[43] Boyle D.P. *et al* 2013 Varying the pre-discharge lithium wall coatings to alter the characteristics of the ELM-free H-mode pedestal in NSTX *J. Nucl. Mater.* **438** S979–82
[44] Podesta M. *et al* 2012 *Proc. 24th Int. Conf. on Fusion Energy (San Diego, CA, 2012)* (Vienna: IAEA) paper EX/P3-02 (www-naweb.iaea.org/napc/physics/FEC/FEC2012/index.htm)
[45] Canik J. *et al* 2011 *Phys. Plasmas* **18** 056118
[46] Boyle D.P. *et al* 2011 *Plasma Phys. Control. Fusion* **53** 105011
[47] Krstic P. *et al* 2013 *Phys. Rev. Lett.* **110** 105001
[48] Houlberg W.A. *et al* 1997 *Phys. Plasmas* **4** 9
[49] Belli E. and Candy J. 2008 *Plasma Phys. Control. Fusion* **50** 095010
[50] Scotti F. *et al* 2013 *Nucl. Fusion* **53** 083001
[51] Maingi R. *et al* 2012 *Nucl. Fusion* **52** 083001
[52] Kotschenreuther M. *et al* 1995 *Comput. Phys. Commun.* **88** 128
[53] Dickinson D. *et al* 2012 *Phys. Rev. Lett.* **105** 135002
[54] Jaworski M. *et al* 2013 *Nucl. Fusion* **53** 083032
[55] Snyder P.B. *et al* 2002 *Phys. Plasmas* **9** 2037
[56] Wilson H.R. *et al* 2002 *Phys. Plasmas* **9** 1277
[57] Huysmans G.T.A. 2005 *Plasma Phys. Control. Fusion* **47** B165
[58] Wilson H.R. *et al* 2006 *Plasma Phys. Control. Fusion* **48** A5
[59] Chang C.S. *et al* 2012 *Proc. 24th Int. Conf. on Fusion Energy 2012 (San Diego, CA, 2012)* (Vienna: IAEA) paper TH/P4-12 (www-naweb.iaea.org/napc/physics/FEC/FEC2012/index.htm)
[60] Maingi R. *et al* 2009 *Phys. Rev. Lett.* **103** 075001
[61] Maqueda R.J. and Maingi R. 2009 *Phys. Plasmas* **16** 056117
[62] Snyder P. *et al* 2011 *Nucl. Fusion* **51** 103016
[63] Lloyd B. *et al* 2011 *Nucl. Fusion* **51** 094013
[64] Diallo A. *et al* 2013 *Nucl. Fusion* **53** 093026
[65] Meyer H. *et al* 2011 *Nucl. Fusion* **51** 113011
[66] Smith D.R. *et al* 2012 *Rev. Sci. Instrum.* **83** 10D502

[67] Smith D.R. *et al* 2012 *Proc. 24th Int. Conf. on Fusion Energy 2012 (San Diego, CA, 2012)* (Vienna: IAEA) paper EX/P7-18 (www-naweb.iaea.org/napc/physics/FEC/FEC2012/index.htm)
[68] Smith D.R. *et al* 2013 *Phys. Plasmas* **20** 055903
[69] Crocker N.A. *et al* 2011 *Plasma Phys. Control. Fusion* **53** 105001
[70] Ku S.-H. *et al* 2009 *Nucl. Fusion* **49** 115021
[71] Yan Z. *et al* 2011 *Phys. Rev. Lett.* **107** 055004
[72] Sabbagh S.A. *et al* 2006 *Nucl. Fusion* **46** 635
[73] Reimerdes H. *et al* 2005 *Nucl. Fusion* **45** 368
[74] Gryaznevich M.P. *et al* 2012 *Nucl. Fusion* **52** 083018
[75] Zhu W. *et al* 2006 *Phys. Rev. Lett.* **96** 225002
[76] Gerhardt S.P. *et al* 2013 *Nucl. Fusion* **53** 043020
[77] Sabbagh S.A. *et al* 2002 *Phys. Plasmas* **9** 2085
[78] Sabbagh S.A. *et al* 2004 *Nucl. Fusion* **44** 560
[79] La Haye R.J. *et al* 2012 *Phys. Plasmas* **19** 062506
[80] Park J.-K. *et al* 2012 *Proc. 24th Int. Conf. on Fusion Energy 2012 (San Diego, CA, 2012)* (Vienna: IAEA) paper EX/P4-33 (www-naweb.iaea.org/napc/physics/FEC/FEC2012/index.htm)
[81] Sabbagh S.A. *et al* 2013 *Proc. 24th Int. Conf. on Fusion Energy 2012 (San Diego, CA, 2012)* (Vienna: IAEA) paper OV/3-1 (www-naweb.iaea.org/napc/physics/FEC/FEC2012/index.htm)
[82] Abdelaziz T.H.S. and Valasek M. 2005 *Proc. 16th IFAC World Congress (Prague, Czech Republic, 2005)* www.ifac-papersonline.net/World_Congress/Proceedings_of_the_16th_IFAC_World_Congress__2005/index.html
[83] Katsuro-Hopkins O. *et al* 2007 *Nucl. Fusion* **47** 1157
[84] Gerhardt S.P. *et al* 2012 *Nucl. Fusion* **52** 063005
[85] Gerhardt S.P. 2013 *Nucl. Fusion* **53** 023005
[86] Hender T.C. *et al* 2010 *Proc. 23rd Int. Conf. on Fusion Energy 2010 (Daejeon, South Korea, 2010)* (Vienna: IAEA) CD-ROM file EX/10-3 and www-naweb.iaea.org/napc/physics/FEC/FEC2010/html/index.htm
[87] Fredrickson E. *et al* 2013 *Nucl. Fusion* **53** 013006
[88] White R.B. and Chance M.S. 1984 *Phys. Fluids* **27** 2455
[89] Menard J.E. *et al* 2006 *Phys. Rev. Lett.* **97** 095002
[90] Cecconello M. *et al* 2012 *Nucl. Fusion* **52** 094015
[91] Kramer G.J. *et al* 2013 *Plasma Phys. Control. Fusion* **55** 025013
[92] Bortolon A. *et al* 2013 *Phys. Rev. Lett.* **110** 265008
[93] Wong K.L. *et al* 1992 *Phys. Fluids* B **4** 2122
[94] Gusev V.K. *et al* 2011 *Nucl. Fusion* **52** 103019
[95] Fredrickson E.D., Gorelenkov N.N. and Menard J. 2004 *Phys. Plasmas* **11** 3653
[96] Gryaznevich M. *et al* 2008 *Nucl. Fusion* **48** 084003
[97] Appel L. *et al* 2008 *Plasma Phys. Control. Fusion* **50** 115011
[98] Belova E. *et al* 2012 *Proc. 24th Int. Conf. on Fusion Energy 2012 (San Diego, CA, 2012)* (Vienna: IAEA) paper TH/P6-16 (www-naweb.iaea.org/napc/physics/FEC/FEC2012/index.htm)
[99] Crocker N. *et al* 2013 *Nucl. Fusion* **53** 043017
[100] Stutman D. *et al* 2009 *Phys. Rev. Lett.* **102** 115002
[101] Hosea J.C. *et al* 2008 *Phys. Plasmas* **15** 056104
[102] Taylor G. *et al* 2010 *Phys. Plasmas* **17** 056114
[103] Perkins R.J. *et al* 2012 *Phys. Rev. Lett.* **109** 045001
[104] Mastrovito D. *et al* 2003 *Rev. Sci. Instrum.* **74** 5090
[105] Jacquet P. *et al* 2011 *Nucl. Fusion* **51** 103018
[106] Perkins R.J. *et al* 2013 *Nucl. Fusion* **53** 083025
[107] Green D.L. *et al* 2011 *Phys. Rev. Lett.* **107** 145001
[108] Ryutov D.D. 2007 *Phys. Plasmas* **14** 064502
[109] Soukhanovskii V.A. *et al* 2013 *J. Nucl. Mater.* **438** S96
[110] Hermann A. *et al* 2003 *J. Nucl. Mater.* **313–316** 759
[111] Federici G., Loarte A. and Strohmayer G. 2003 *Plasma Phys. Control. Fusion* **45** 1523
[112] Soukhanovskii V.A. *et al* 2011 *Nucl. Fusion* **51** 012001
[113] Soukhanovskii V.A. *et al* 2012 *Proc. 24th Int. Conf. on Fusion Energy 2012 (San Diego, CA, 2012)* (Vienna: IAEA) paper EX/P5-21 (www-naweb.iaea.org/napc/physics/FEC/FEC2012/index.htm)
[114] Ryutov D.D. *et al* 2012 *Proc. 24th Int. Conf. on Fusion Energy 2012 (San Diego, CA, 2012)* (Vienna: IAEA) paper TH/P4-18 (www-naweb.iaea.org/napc/physics/FEC/FEC2012/index.htm)
[115] Sabbagh S.A., Bell R.E. and Menard J.E. 2006 *Phys. Rev. Lett.* **97** 045004
[116] Canik J. *et al* 2010 *Phys. Rev. Lett.* **104** 045001
[117] Eich T. *et al* 2003 *Phys. Rev. Lett.* **91** 195003
[118] Buttery R. *et al* 1996 *Nucl. Fusion* **36** 1369
[119] Evans T.E. *et al* 2005 *J. Phys.: Conf. Ser.* **7** 174
[120] Schmitz O. *et al* 2008 *Plasma Phys. Control. Fusion* **50** 124029
[121] Jakubowski M.W. *et al* 2009 *Nucl. Fusion* **49** 095013
[122] Ahn J.-W. *et al* 2012 *Proc. 24th Int. Conf. on Fusion Energy 2012 (San Diego, CA, 2012)* (Vienna: IAEA) paper EX/P5-33 (www-naweb.iaea.org/napc/physics/FEC/FEC2012/index.htm)
[123] Gan K.F. *et al* 2013 *Rev. Sci. Instrum.* **84** 023505
[124] Ahn J.-W. *et al* 2011 *Phys. Plasmas* **18** 056108
[125] Feng Y. *et al* 1997 *J. Nucl. Mater.* **241-243** 930
[126] Reiter D. *et al* 2005 *Fusion Sci. Technol.* **47** 172
[127] Canik J. *et al* 2011 *J. Nucl. Mater.* **415** S409
[128] Lore J.D. *et al* 2012 *Nucl. Fusion* **52** 054012
[129] Maingi R. *et al* 2010 *Nucl. Fusion* **50** 064010
[130] Kaye S.M. *et al* 2011 *Nucl. Fusion* **51** 113019
[131] Chang C.S. *et al* 2002 *Phys. Plasmas* **9** 3884-92
[132] Maingi R. *et al* 2004 *Plasma Phys. Control. Fusion* **46** A305-13
[133] Raman R. *et al* 2011 *Phys. Plasmas* **18** 092504
[134] Raman R. *et al* 2013 *Nucl. Fusion* **53** 073017
[135] Taylor G. *et al* 2012 *Phys. Plasmas* **19** 042501
[136] Gerhardt S.P. *et al* 2012 *Nucl. Fusion* **52** 083020
[137] Gerhardt S.P. *et al* 2011 *Nucl. Fusion* **51** 073031
[138] Kaye S.M. *et al* 2006 *Nucl. Fusion* **46** 848